Experimental study of gas-lift systems with inclined gas jets

L.A.O. Guerra [b], B.O. Temer [c], J.B.R. Loureiro [a,b,c,*], A.P. Silva Freire [a,b]

[a] Interdisciplinary Center for Fluid Dynamics (NIDF/UFRJ), R. Moniz Aragão 360, 21941-594, Rio de Janeiro, Brazil
[b] Mechanical Engineering Program (PEM/COPPE/UFRJ), Brazil
[c] Mechanical Engineering Department (DEM/Poli/UFRJ), C.P. 68503, 21941-972, Rio de Janeiro, Brazil

ARTICLE INFO

ABSTRACT

The focus of the present research is on the optical measurements of gas jets in liquid cross flows in vertical pipes. Three distinct injection angles (-45°, 0°, 45°), two orifice diameters (2 and 5 mm) and air and water flow rates varying respectively between 0.57 to 2.15 m^3h^{-1} and 2 to 5 m^3h^{-1} were investigated. To characterize the continuous and dispersed flow phases, shadow sizing and particle image velocimetry (two well-established optical measurement techniques) were employed. Global and local measurements provide data on the bubble diameter distribution, bubble shapes, air jet deflection angles, mean velocity profiles in the continuous phase and pressure distributions. The work compares the different features associated with the three angles of injection to determine the most appropriate geometry for a desired application. The diameter distributions for small bubbles appear to be insensitive to the liquid and gas flow rates and to the diameter and angle of the gas injector. The size distributions of the large bubbles, however, depend strongly on the flow parameters and the geometry of the injector (diameter and angle). The measured mean velocity profiles illustrate the complex interactions between the continuous and dispersed phases and the pipe wall.

1. Introduction

Gas-lift systems respond for an estimated 70% of Brazil's offshore oil production (Plucenio et al., 2012). This compelling fact has motivated the oil industry to develop innovative and optimized technologies to improve field production. Recent studies have explored new developments in sensor know-how, control equipment and data transmission to propose important breakthrough technologies including automated system for the integrated operation of gas-lift platforms (Nishikiori et al., 1995; Camponogara et al., 2010; Bezerra et al., 2019; Mahdiani et al., 2019).

To maintain production at an expected rate over the entire economic life of an oil well, gas and water are normally injected to increase pressure in depleted reservoirs. Additionally, complementary techniques are used to ensure that further necessary energy is transferred downhole. One relevant engineering problem is hence the determination of the proper type of artificial lift technique to be applied to a known field. The four commonest techniques are sucker rod pumps, submersible pumps, hydraulic pumps or gas-lift systems.

Gas-lift systems resort to the injection of high-pressure gas to reduce the fluid density and the column weight, so that the pressure differential between the reservoir and the wellbore is increased. In view of their simplicity, reliability and flexibility, gas-lift systems are extensively used in industry. Their design selection, however, is not straightforward. Several aspects including economical, technological, geographical and environmental issues must be considered for the best possible choice. Gas-lift systems closely resemble natural flows. They are adaptable to changes in reservoir conditions and are beneficial for high production rates. They can also handle large volumes of solid particles and can function under various operational conditions with essentially the same well equipment. Their power source is remotely located and the valves can normally be serviced without disturbing the tubing. A major problem of gas-lift facilities is the installation of small casing sizes, which may limit the system to small tubing diameters and pumping equipment, hence resulting in small gas flow rates. According to Brown (1982) gas-lift mandrels normally accept 25 mm OD gas-lift valves. Optimization of the gas-lift valve is thus a crucial aspect of any successful air-lift system designed for oil wells.

The present work studies the effects of bubble size on gas-lift systems, in an approach that bears much methodological resemblance to the works of Guet (2004), Khalil et al. (1999), Hu et al. (2012) and Ahmed et al. (2016). The objective is to study, through optical measurements, the possible effects of the injection angle on the performance of gas-lift systems fitted with single nozzle injectors. The two key optical measurement techniques employed in the experiments are Shadow Sizing (SS) and Particle Image Velocimetry (PIV). Important

---

issues that are not often addressed in the literature are thoroughly discussed here. These include the effects of the injection angle on the resulting flow configuration (pattern and sizes of bubbles) and pressure decrease. Generally, the smaller the sizes of generated bubbles, the better is the performance of a gas-lift system. Here, we study the flow properties resulting from a single nozzle injector inclined at angles γ = −45° (opposite-flow direction), 0° (orthogonal-flow direction) and 45° (matching-flow direction) to the main pipe flow. Two nozzle diameters (2 and 5 mm) are considered in the study of vertical flows of water (2 and 5 $m^3 h^{-1}$) and air (0.57 and 2.15 $m^3 h^{-1}$). The properties of the dispersed phase are determined through Shadow Sizing (SS). The optical SS-measurements furnish data on the flow patterns, the statistics of bubble size and shape and the air-jet deflection angle. The mean velocity profiles of the continuous phase are characterized through Particle Image Velocimetry (PIV). In all, 18 different data sets are analyzed.

Studies on bubble formation, interaction, coalescence and breakup due to gas injection into a liquid cross flow in a vertical pipe are rare in the literature. Most works discuss bubbles in horizontal flows (Marshall, 1990; Marshall and Chudasek, 1993; Chen and Richter, 1997; Matas et al., 2011; Balzan et al., 2017; Rek et al., 2017; Ma et al., 2021; Dhar, 2021). Investigations on the effects of the angles of injection and orifice diameter on flow properties are also rare. The present work provides vital data on bubble and flow statistics that are crucial for the performance evaluation of gas-lift devices and their design. The work not only discusses the different flow patterns occurring (single bubbling (SB), pulse bubbling (P), elongated jetting (EJ) and atomizing jet (AJ)) but also offers quantitative data on bubble features and flow properties.

The experiments show that the size distributions for small bubbles seem to be insensitive to the liquid and gas flow rates and to the diameter and angle of the gas injector. The only exception are the cases of orthogonal injection and the 5-mm injector where a relative increase in the number of small bubbles is observed. An increase in the liquid flow rate (and consequently, the turbulence level) results in an increase in the number of small bubbles as expected. The size distributions of the large bubbles on the other hand seem to depend substantially on the flow parameters and the geometry of the injector (diameter and angle). The matching-flow injection is observed to produce larger bubbles (with a higher average equivalent diameter). Expected features such as an increase in equivalent bubble diameter (d_{eq}) with an increase in the injector diameter were observed. For a given gas flow rate, the 2-mm injector produced about three times more small bubbles than the 5-mm injector (which generated more large bubbles). The measured mean velocity profiles illustrate the complex interaction between the continuous and dispersed phases, highlighting the roles of the gas and liquid flow rates. Changes in the local pressure due to the injection angle were minor.

The large number of flow controlling parameters (the flow rates of water and air, the internal diameter and angle of the injection pipe, the diameter of the conveying pipe) imply that any meaningful physical interpretation of the problem would naturally require a large number of data to be retrieved and processed. A further complication for data interpretation results from the observed complex flow patterns where small and large bubbles freely interact with each other and with the pipe wall. The experimental characterization of bubble morphology in dense bubble flows is notoriously difficult (Ferreira et al., 2012; Lau et al., 2013; Karn et al., 2015) due to many factors. While many of the difficulties related to the position and quality of light and image focus can be worked out, a more difficult issue is the correct identification of isolated, visually overlapping and clustered bubbles. In the present study, the lack of flow symmetry introduced a further complexity, since side and front views of the flow depending on the considered configuration could eventually result in different bubble identification. Therefore, data sets for both side and front views were obtained for *all* flow conditions and were individually compared for consistency.

A short review of previous works on gas-lift is presented next (Section 2). The experimental setup and flow conditions are introduced in Section 3. The flow pattern results are presented in Section 4 (size and shape of bubbles, jet deflection). Section 5 discusses mean velocity profiles for the liquid phase and the pressure distributions. Section 6 concludes the work. The fluid mechanics of gas-lift systems is briefly discussed in Appendix A. The purpose of this part of the appendix is to fix notation and clarify concepts, in particular the physical contributions to the pressure difference term (gravity, friction, acceleration). The bubble size statistics according to the viewing angle are shown in Appendix B.

2. Gas-lift systems

2.1. Problem definition

Different constraints imposed by the many existing applications often limit the way in which a gas is injected into a fluid. In general, in air-lift pumps the injection of bubbles is less troublesome and can be made through extended porous surfaces or nozzles with multiple holes, arranged in configurations that can be vertical or horizontal, annular, detached or flush with the wall. Bubbles in many cases may have the option of being injected radially, axially, in combined arrangements (radial and axial), with swirl or in a spatially distributed manner.

For gas and oil wells in an offshore environment, the efficiency of a gas-lift system is highly influenced by the depth of the operating device (valve), and installation and operating constrains are very severe. The greater the depth, the more of the hydrostatic pressure of the heavier fluid column is taken off of the formation, reducing the bottom hole pressure and increasing production.

To install gas-lift systems at great depths, a series of unloading valves need to be used. These valves are placed at different depths and have their opening and closing pressure settings adjusted to step the gas injected into the annular pipe down to the desired depth.

Gas-lift valves are fitted into mandrels that are installed at the surface as part of the tubing stream. Two types of mandrels are of common use: (i) conventional mandrels with threaded non-retrievable valves, and (ii) side pocket mandrels (SPMs) with retrievable valves. The latter mandrels have an internally offset pocket that can be accessed through the tubing with the use of wireline tools. This feature is very convenient, for it permits the installation and retrieval of different types of gas-lift valves for production optimization and well maintenance.

In side pocket mandrels, the design of the gas-lift valve is such as to promote the flow of gas into the tubing in the downward or orthogonal directions (Fig. 1) through single ports with sizes varying between 3 to 10 mm. In fact, most of the injectors currently used in industry normally inject gas through a single nozzle in an opposite-flow configuration.

2.2. Comments on some previous works on gas-lift systems

Studies on vertical two-phase flows are abundant in literature. The reader is referred to the works of Wallis (1969), Govier and Aziz (1977), Clift et al. (1978) and Brennen (2005) for an overview of the subject. More specific treatments can be found in many review articles, including the works of Magnaudet and Eames (2000) and Balachandar and Eaton (2010).

Air-lift *pumps* are based on working principles that are closely related to those in gas-lift *systems*. Several works are found in the literature where the effects of pipe diameter, gas injection method and pipe enlargement (step or continuous) are studied (Reinemann et al., 1990; de Cachard and Delhaye, 1996; Khalil et al., 1999; Hu et al., 2012; Ahmed et al., 2016). The consensus is that air-lift pumps operate best in the slug flow pattern.

For gas-lift systems, the work of Guet (2004) concludes that the reduction of bubble size improves the efficiency of gas injection since the lower velocities result in a larger residence time with a consequent
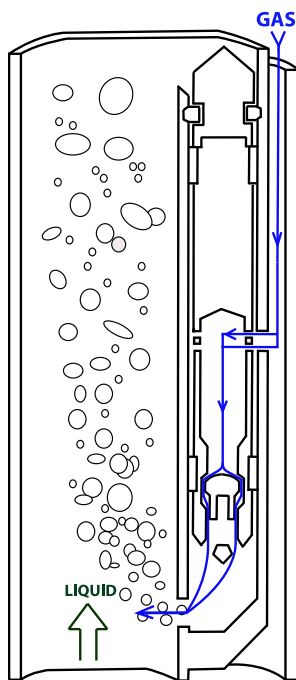
Fig. 1. Side pocket mandrel with gas-lift valve.

larger average void fraction. Guet discusses four types of gas injection systems to further show that the concentration distributions of generated bubbles have a strong influence on the transition of flow regime, from bubbly to slug. The effects of gas injection on the fluid mechanical aspects of gas-lift techniques are also discussed in Guet and Ooms (2006).

Gas-lift systems with particular application to oil fields are reviewed by Ayatollahia et al. (2004). According to these authors, the production from fields can be significantly increased through intermittent gas injection. More applied works by Redden et al. (1974), Palke (1996) and Wang and Litvak (2004) have discussed gas-lift optimization for reservoir simulations. The optimization problem, of course, depends on the multiphase simulations of compositional fluid flow in the reservoir, the pipeline network and separation equipment.

2.3. Gas fraction profile

In a series of papers, Serizawa et al. (1975a,b,c) described the turbulence structure of vertical air–water bubble flows. Using dual-sensor resistivity probes, the authors showed that the radial gas fraction profiles changed from a saddle (bubble flow) to a parabolic (slug flow) configuration depending on the gas flow rate. The mean velocity profile of the bubbles was observed to follow a power-law expression in the radial direction.

Liu and Bankoff (1993a,b) also investigated the flow structure of vertical air–water bubble flows. The local velocities and turbulent stresses of the liquid-phase were measured through laser Doppler velocimetry. The results showed that (i) an increase in Q_G (at constant Q_L) increases the turbulent quantities, and (ii) an increase in Q_L (at constant Q_G) reduces the liquid phase turbulence in the core region of the pipe, but increases the turbulence in the wall region. Using a miniature dual-sensor resistivity probe, measurements of the radial profiles of gas fraction, bubble velocity and size were presented. The gas fraction and bubble size distributions in the radial direction essentially confirmed the findings of Serizawa et al. (1975b). The test conditions showed a marked peak for the gas fraction near the wall and a relatively flat behavior in the core region. Further recent modeling

on the dynamics of gas–liquid flows has been provided by Wang et al. (2021).

Many relevant works followed the above referred papers; the general trends described in these publications, however, remained essentially unchanged over the years. Recent important contributions on the dynamics of bubble columns can be found in the works of Lehr et al. (2002), Kaji et al. (2009), Lucas et al. (2010) and Qi et al. (2012).

2.4. Bubble formation from orifices with liquid cross-flow

The simplest way to form a bubble is at a circular orifice facing upward in a quiescent fluid. This is a classical problem that has been extensively discussed in the literature (see, e.g., Tavlarides et al. (1970)). Despite some surprising complications, potential flow theory has proven to be a successful tool for description of this problem.

The conditions for bubble formation from an orifice in a plane wall with transverse liquid flow, however, have received considerable less attention. Marshall and Chudasek (1993) extends the use of previously developed potential flow theory to account for the transverse motion of a bubble.

An important study on bubble formation regimes was introduced in Balzan et al. (2017) for gas injection into a liquid cross flow in a horizontal square channel. Three different injection diameters were tested. High-speed visualization was used to identify four flow regimes: single bubbling (SB), pulse bubbling (P), elongated jetting (EJ) and atomizing jet (AJ). Single bubbling regime refers to the creation of individual bubbles of nearly spherical shapes at regular intervals, resulting in bubble size distributions that are essentially monodisperse. In the pulsating regime, a chain of discernible but interconnected bubbles is produced. The slender necks that are repeatedly produced between bubbles give the appearance that the gas is pulsating. A continuous increase in the gas flow rate eventually leads to the appearance of a continuous jet. In some studies continuous jets are further classified either as elongated jets (a jet whose length is considerably greater than the pipe diameter) or atomizing jets (where bubble formation is disorganized and bubble morphology shows large variations).

Two-dimensional numerical simulations were performed by Prasad et al. (2018) to analyze the effects of two adjacent orifices on the formation and evolution of bubbles in stagnant and co-flowing liquids. The volume-of-fluid method was used to capture bubble growth, neck formation and bubble coalescence and breakup.

Rek et al. (2017) performed three-dimensional numerical simulations of gas–liquid jets in a horizontal cross-flow. To track the interfaces, a volume-of-fluid method was used. Turbulence modeling was achieved through a one-equation eddy viscosity model for implicit LES. The simulations were compared to experimental data and used to propose correlations for prediction of the jet deflection angle.

One of the few available works in the literature to study the effects of orifice and flow orientation on bubble formation is the paper of Liu et al. (2013). Four types of orientation effects were discussed. A horizontal orifice in a vertically upward liquid flow was concluded to form the smallest bubbles. For small enough orifices or liquid flow velocities over 3.2 ms^{-1} the orientation effects were found to be insignificant.

Integral theoretical models based on global force balances continue to show their usefulness in predicting bubble detachment from a wall orifice in cross-flow. The recent work of Ma et al. (2021) accounts for the liquid inertia, drag, surface tension, shear lift, pressure, buoyancy and gas momentum forces to derive a simple model for estimation of bubble detachment.

Dhar (2021) used optical sensors to measure the sizes and velocities of bubbles issuing from two orifice geometries in a horizontal channel. Both the sizes and velocity distributions of bubbles were observed to follow a log-normal distribution. An increase in gas flow rates was observed to increase the sizes and velocities of the large bubbles. Flow visualization was obtained using a high speed camera.

For an excellent review on bubble formation and bubble rise velocity in gas–liquid systems we recommend the review paper of Kulkarni and Joshi (2005).
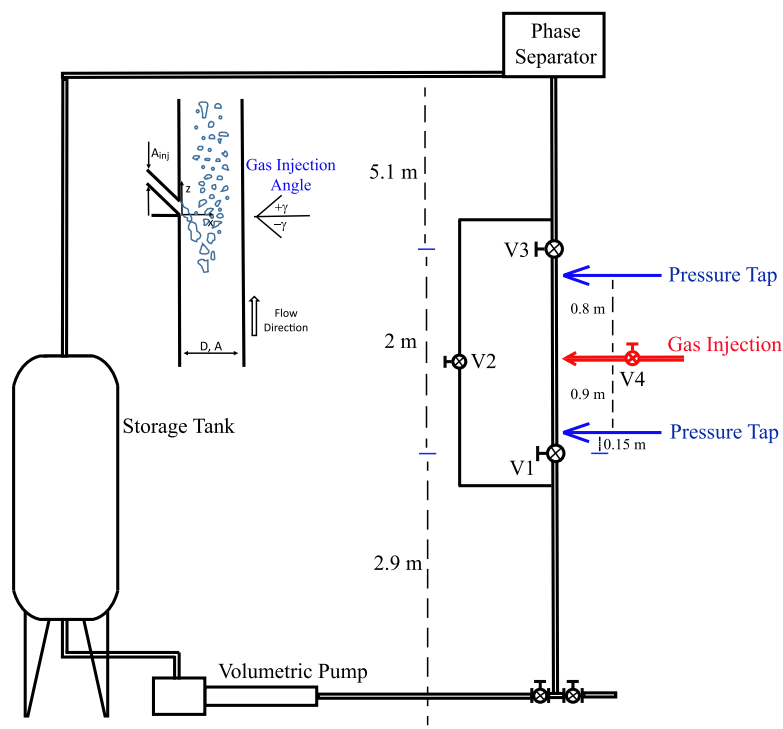
Fig. 2. Schematic diagram of the experimental set up. Injection angle definition (inset).

3. Experimental set-up and instrumentation

The present experiments were performed in a Plexiglas vertical pipe having a length of 10 m and an internal diameter of 44 mm. A schematic diagram of the experimental apparatus is shown in Fig. 2. The pipe is part of an open loop that begins with a 4 m^3 water storage tank. A progressive cavity pump is used to move water from the storage tank to the test section. The gas flow is provided by a compressor with a dryer to remove humidity. The liquid and gas flow rates are controlled by an electromagnetic flow meter and a calibrated rotameter. The differential pressure was measured with a differential transducer. At the top of the circuit, a separator diverts the collected water to the storage tank and releases the air to the atmosphere.

The test section is located 4 m above ground level. Measurements were conducted using two optical techniques: Shadow Sizing (SS) and Particle Image Velocimetry (PIV). For the PIV and SS measurements a transparent box filled with water was used to eliminate optical distortions. In the interior of the box and flush with the wall, nozzles with 2 or 5 mm internal diameter were installed for the gas injection. The nozzle could be positioned in three different configurations, at directions 45° (matching-flow), 0° (orthogonal) and −45° (opposite-flow) relative to the main flow (see Fig. 2). Four fast-closing valves were used to estimate the gas holdup. Once the gas supply valve (V_4) was closed, valves at the two ends (V_1 and V_3) of the test section were simultaneously closed. A valve (V_2) was used to open the by-pass section to permit water to flow through the open loop. The position of the valves, pressure taps and gas injection point are shown in Fig. 2.

To characterize the pressure changes with different liquid and gas flow rates at different injection angles, seven pressure taps were distributed below and above the gas injection point (two are shown in Fig. 2). Measurements were taken once all valves in the main circuit were open and the water pump and air injection system furnished a steady flow.

The test conditions for the 2 and 5 mm injectors are shown in Table 1.

Table 1
Test conditions. d_{inj} and γ are the internal diameter and the inclination in relation to the main flow of the jet nozzle. −45° = opposite-flow direction; 0° = orthogonal-flow direction; 45° = matching-flow direction.

d_{inj} (mm)	γ (°)	Q_L (m^3 h^{-1})	Q_G (m^3 h^{-1})
2	−45	2	0.57
2	0	2	0.57
2	45	2	0.57
2	−45	2	2.15
2	0	2	2.15
2	45	2	2.15
2	−45	5	0.57
2	0	5	0.57
2	45	5	0.57
2	−45	5	2.15
2	0	5	2.15
2	45	5	2.15
5	−45	2	0.57
5	0	2	0.57
5	45	2	0.57
5	−45	5	2.15
5	0	5	2.15
5	45	5	2.15

3.1. Shadow sizing technique

The Shadow Sizing technique made use of the same procedure and equipment described in Matamoros et al. (2014), Celis et al. (2021) and Rosero et al. (2022).

This technique is based on the capture of high-resolution images with pulsed background illumination. The objects to be identified (bubbles, in the present application) must be placed between a diffusive light source and a digital camera (for the present case, a 12 bit Speed Sense M310 camera, with 1280 × 800 pixel resolution and maximum acquisition rate of 3260 frames per second). The acquired images are processed with an advanced algorithm to detect the contours of the bubble and to extract the desired information of identified objects. The
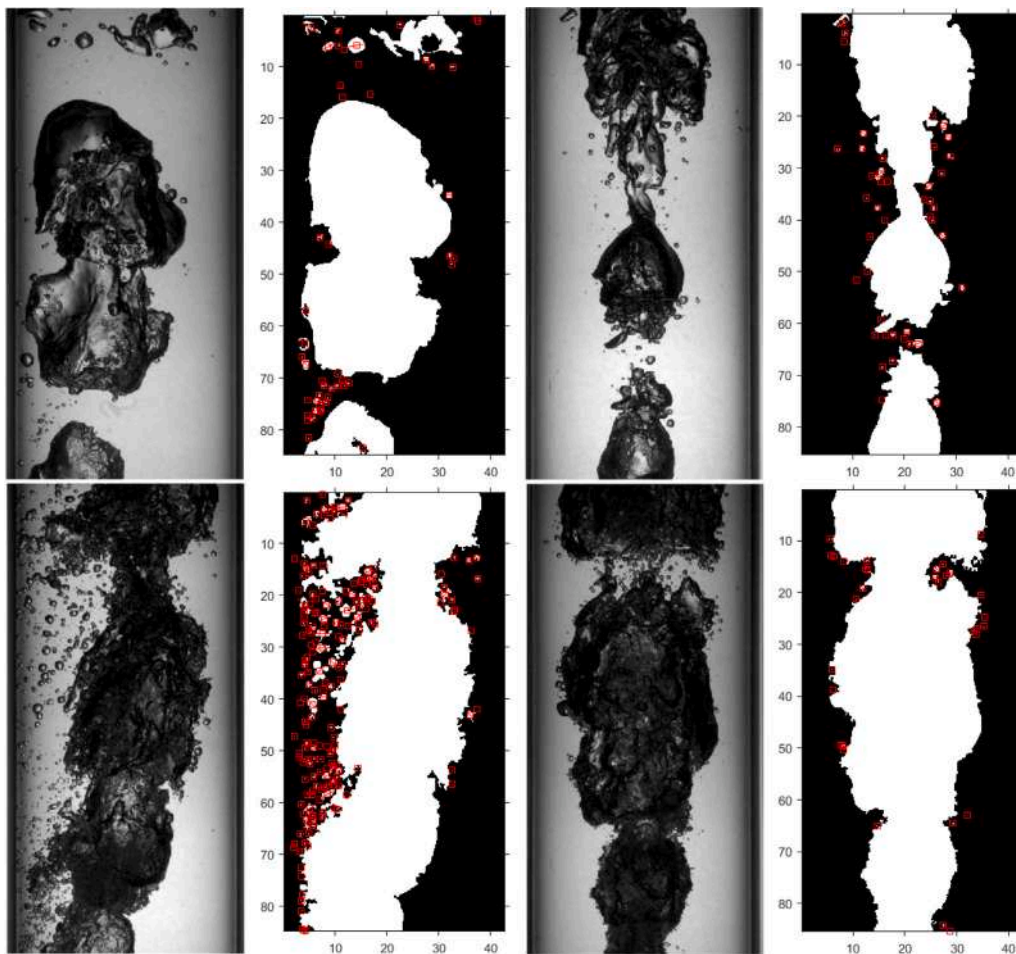
Fig. 3. Contour detection of small bubbles. Side (left) and front (right) views. The injector diameter is $d_{inj} = 2$ mm. Top images: $Q_L = 2$ m³ h⁻¹, $Q_G = 0.57$ m³ h⁻¹; bottom images: $Q_L = 5$ m³ h⁻¹, $Q_G = 2.15$ m³ h⁻¹.

two led systems were placed behind a diffuser installed at the back of the transparent box to provide uniform background illumination.

For image processing, the following software were used: Dynamic Studio™ (from DANTEC Dynamics), MATLAB, ImageJ and Python. The MATLAB and Python software were developed in-house for dedicated contour detection and data processing. The methodology introduced in Nogueira et al. (2003) was typically used here for image treatment. To sharpen and accurately detect the edge of bubbles, a sequence of image processing operations was implemented including subtraction of the mean background and correction of non-uniform brightness.

For convenient image processing, bubbles were classified into the following ranges: small ($d_{eq} < 1.5$ mm), small-medium ($1.5 < d_{eq} < 5$ mm), medium ($5 < d_{eq} < 20$ mm) and large bubbles (20 mm $< d_{eq}$). This classification was arbitrary and aimed at facilitating the application of the available software. In the section on results, reference is made to small ($d_{eq} < 5$ mm) and large bubbles (5 mm $< d_{eq}$).

The correct identification of overlapped and clustered bubbles is normally very difficult in view of the resulting very complex geometric structures and the varying image intensity gradients resulting from in and out-of-focus bubbles (Ferreira et al., 2012; Fu and Liu, 2016). In the present work, isolated small and small medium bubbles – which were counted in great numbers – were automatically identified, but human intervention was always considered for a final check. Medium and large size bubbles were always individually processed.

The frame rate, the exposure time, the illumination time and the magnification were optimized to avoid blur and to furnish adequate

spatial and temporal resolutions. The typical relative overall uncertainty with a confidence interval of 90% for the sizes of the small bubbles was 1 to 11.5%. The maximum relative overall uncertainty with a confidence interval of 90% for the lengths of large bubbles was 0.5%. For a detailed discussion on the measurement uncertainties, please, refer to Celis et al. (2021) and Rosero et al. (2022).

Typically, 2000 to 6000 snapshots were considered for the statistics of the small bubbles. For the large bubbles, 100 to 400 snapshots were considered. Care was taken to prevent a given bubble from being considered multiple times in the statistical computations. For all statistics, bubble counting was made using side and front views of the flow as illustrated in Fig. 3. The viewing window was thus 44×88 mm in width and height. The reason for that was clear. Depending on the flow configuration, and the manner in which the flow asymmetry is manifested, it could be that a particular viewing angle could be less (or more) favorable for the identification of a certain group of bubbles. In particular, it could be that small bubbles would be hidden by large bubbles. This aspect is discussed in detail in the Appendix B.

3.2. Particle image velocimetry

The present PIV measurements used the same configuration in Celis et al. (2021), Rosero et al. (2022) and Magalhães et al. (2013). The specific procedure and technical details can be obtained directly from
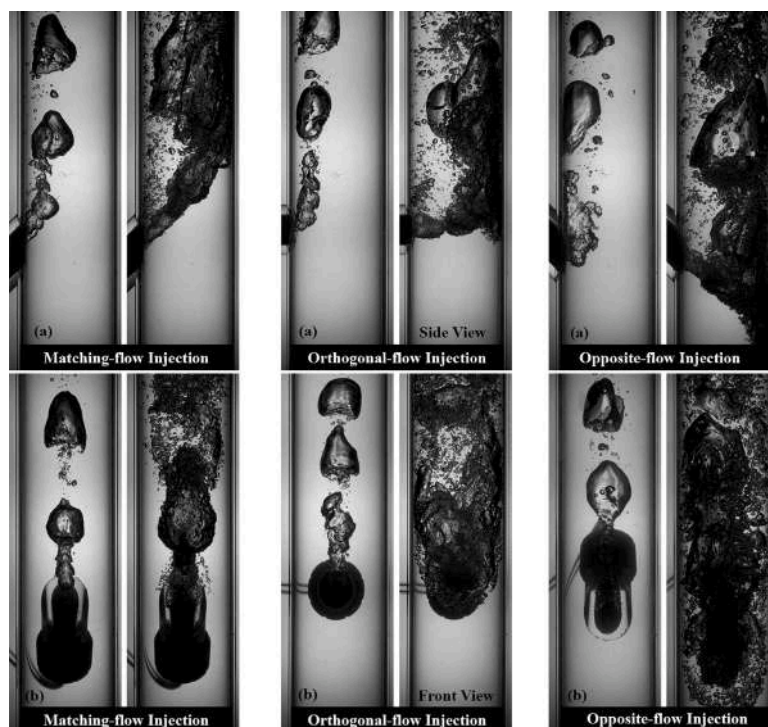
Fig. 4. General flow patterns for the three injection angles. (a) Side view. (b) Front view. The injector diameter is $d_{inj} = 2$ mm. For the low flow rates (image on the left in each pair): $Q_L = 2$ m³ h⁻¹, $Q_G = 0.57$ m³ h⁻¹; for the high flow rates (image on the right in each pair): $Q_L = 2$ m³ h⁻¹, $Q_G = 2.15$ m³ h⁻¹.

these references. Here, for the sake of completeness, a brief general description of the system is presented in the next paragraphs.

The 2D PIV system used the same camera of the Shadow Sizer System with a Litron Nd-Yag laser of 135 mJ and 15 Hz repetition rate. A vertical laser lightsheet was positioned at the pipe center-line, opposite to the injector. A camera is positioned perpendicular to the light sheet to acquire global and sequential images of the flow. Neutrally buoyant fluorescent Rhodamine painted polystyrene particles were used as tracers. As these particles reflect light in the yellow–orange wavelength (572 to 594 nm), the use of a narrow-band 570 nm optical filter in front of the camera lens prevent the bright reflections from the bubble surface from being captured by the PIV images. As suggested by Nogueira et al. (2003) to improve the resolution and accuracy of the liquid velocity estimate near the bubble surface, the backlight led illumination was used simultaneously to the PIV system. To enhance the contrast of the bubble shape, the led systems were covered by a red transparent film and emitted simultaneously to the laser source. The led systems were kept at the same position, in front of the camera, promoting an uniform PIV image with enhanced bubble contour. The contour detection algorithm applied to the PIV images with background illumination (PIV+SS) provided the masks needed to remove information of the gas phase, so that the PIV correlation could be applied solely to the regions where tracer particles were visible.

Details on the presently used 2D-PIV system including features of the hardware and software are particularly described in Celis et al. (2021). The Dynamic Studio software (version 2015a) was used for system synchronization, image acquisition and processing. The camera was triggered in double frame mode. Typically 2000 image pairs were considered for velocity characterization.

4. Flow pattern

As mentioned by Balzan et al. (2017), previous works have struggled to establish a universal system for flow pattern classification of bubble formation in liquid cross-flow. However, an apparent consensus exists as to classify the main regimes into single bubbling, pulsating and jetting. In the present work, low gas flow rates tended to produce pulse bubbling regimes, whereas high gas flow rates gave rise to jetting regimes (elongated and atomizing jets). This picture, however, is incomplete since mixed regimes (a combination of two of the above regimes) were also observed. This is discussed next.

4.1. Bubble fragmentation

The general flow patterns for the three injection angles are shown in Fig. 4 for typical low and high flow rates (air and water).

For the low flow rates, the formation of large bubbles right at the exit region of the nozzles can be clearly observed. The sizes of the bubbles are insensitive to the orientation of the nozzles, and they initially rise close to the wall. Small bubbles can also be observed, but the flow dynamics is dominated by the large bubbles. The observed flow pattern appears to be independent of the injection angle and are of "pulse bubbling" type.

For the higher gas flow rates, the strength of the gas jet is large enough in all flow configurations to provoke an impact of the jet on the opposite pipe wall, giving rise to flow patterns that are strongly dependent on the injection angle. The formation of large bubbles on the wall is notable (in particular from the front view plane) as well as the formation of many small bubbles. The small bubbles result from the shearing action of the cross liquid flow (mainly close to the nozzles) and fragmentation due to turbulence effects and the interaction of the jet with the opposing wall. In the −45° gas-injection configuration, a swarm of small bubbles is observed in a region near the opposite wall, upstream of the jet core. The flow pattern here appears to be of the "atomizing jet" type.

The fragmentation of the incoming gas jet into large bubbles as a result of the interaction with the cross liquid flow is very complex. Fig. 5 shows time sequences of the breakup and coalescence processes
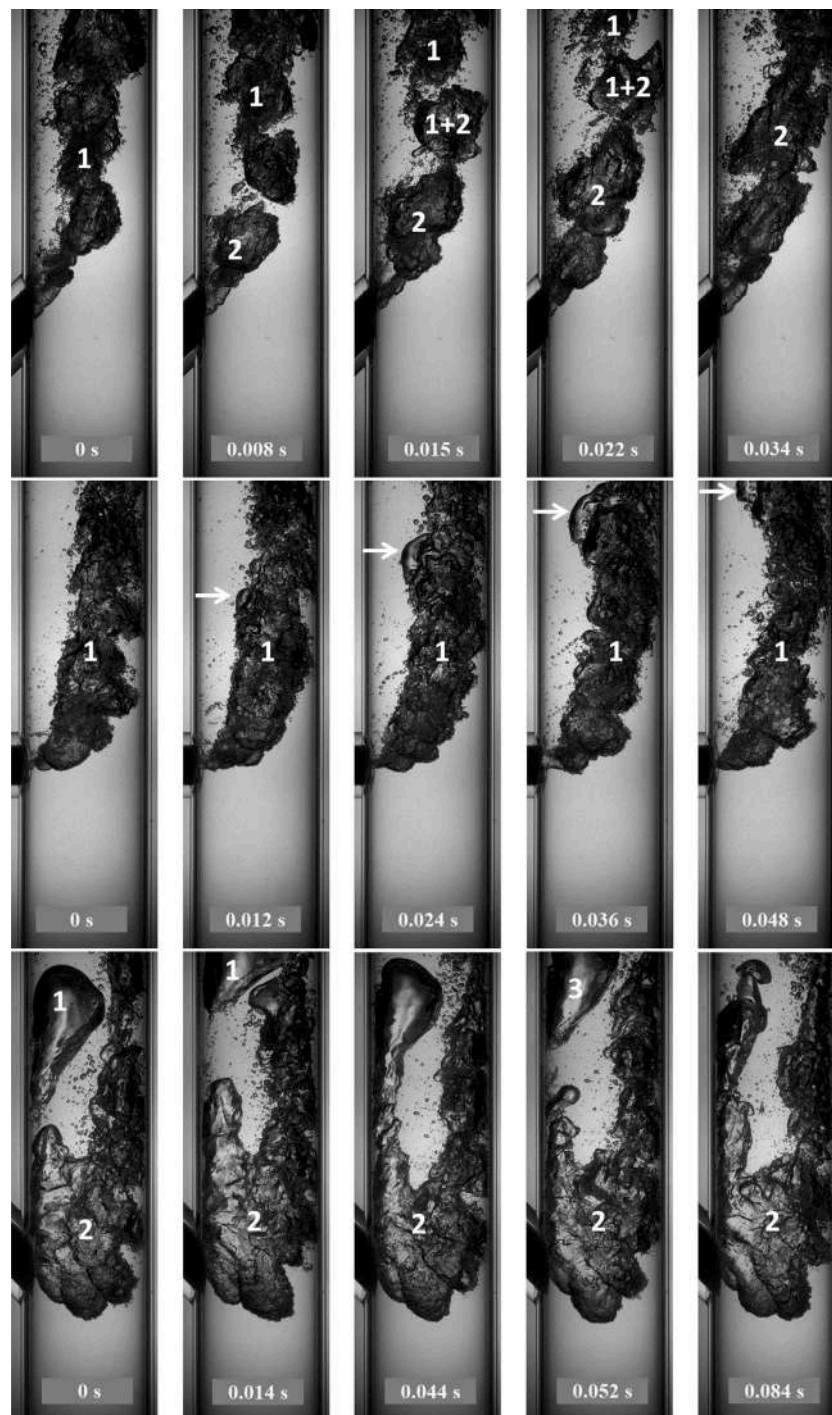
Fig. 5. Flow patterns for d_{inj} = 2 mm, Q_L = 2 m³ h⁻¹, Q_G = 0.57 m³ h⁻¹ and the three injection angles: γ = 45°, 0° and −45°.

of large bubbles for the three injection angles and low flow rates (Q_L = 2 m³ h⁻¹, Q_G = 0.57 m³ h⁻¹) for the 2-mm injector. In all configurations, and as an effect of the cross flow, the gas jet immediately bends and breaks into large bubbles as it leaves the issuing nozzle. For the 45° injection angle, large bubbles are formed which subsequently further disintegrate in a very violent process that results in the appearance of many moderate and small size bubbles. For the orthogonal injection, the process is similar but coalescence of large bubbles is observed mainly due to wake effects. The −45° injection angle, on the other hand, seems to produce moderate large bubbles that soon coalesce

to result in large bubbles. In all pictures, thin necks can be observed connecting clusters of large bubbles. The injection angles apparently do not have much influence on the flow pattern.

For the highest injection rates (Fig. 6, Q_L = 5 m³ h⁻¹, Q_G = 2.15 m³ h⁻¹), the flow configurations show significant changes. The flow appears to be in the "jetting pattern" regime, but relevant differences are observed at different injection angles. The large gas flow rate tends to generate a train of large bubbles that are set very close together and surrounded by many tiny bubbles. This tendency is clearly shown in Fig. 6. For the 45° injection, the breakup of large bubbles is

Fig. 6. Flow patterns for d_{inj} = 2 mm, Q_L = 5 m³ h⁻¹, Q_G = 2.15 m³ h⁻¹ and the three injection angles γ = 45°, 0° and −45°.

observable. The bubbles are highly distorted but cohesive chunks of gas are easily identified. In the orthogonal gas injection, the stream of gas seems almost continuous. In fact, for any given instance, some portions of the gas seem to form apparently stable structures, which are, however, quickly squashed into each other through the forces involved

in the phenomenon. For the −45° injection, the gas jet interacts with the main flow in a very peculiar way. A large volume of gas spans the pipe diameter and a relatively stable pattern is observed. This volume of gas periodically releases very large bubbles adjacent to the near wall. On the far wall, a permanent pattern formed by large, moderate
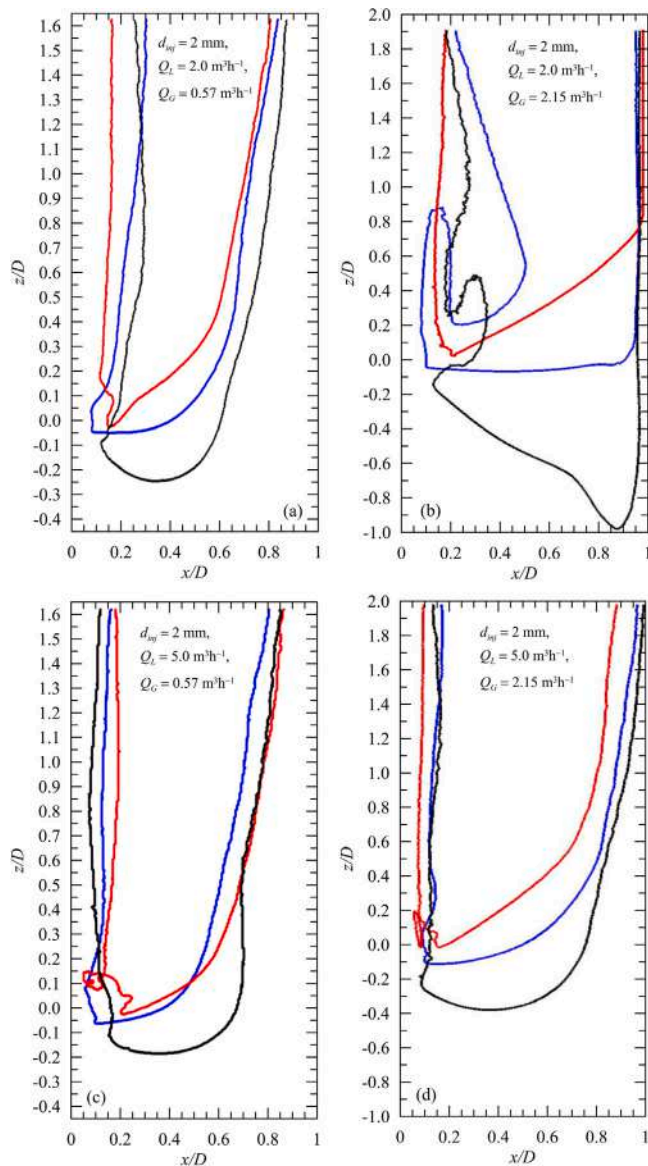
Fig. 7. Illustration of the relative gas-jet deflection for d_{inj} = 2 mm. (a) Q_L = 2 m³ h⁻¹, Q_G = 0.57 m³ h⁻¹; (b) Q_L = 2 m³ h⁻¹, Q_G = 2.15 m³ h⁻¹; (c) Q_L = 5 m³ h⁻¹, Q_G = 0.57 m³ h⁻¹; (d) Q_L = 5 m³ h⁻¹, Q_G = 2.15 m³ h⁻¹. Red lines: matching-flow injection. Blue lines: orthogonal-flow injection. Black lines: opposite-flow injection.

and small bubbles is observed. This flow configuration appears to be a combination of two of the normally classified flow patterns: pulse bubbling and atomized jet.

4.2. Gas-jet deflection

The deflection of the gas jet due to the action of the cross flow is greatly affected for the 2-mm injector. The small diameter implies that the momentum flux leaving the jet for the highest gas flow rate is 0.14 N (= $\rho_g A_{inj}^{-1} v_g^2$, where v_g is the volumetric gas flow rate). This value is large enough to allow the gas jet to penetrate deeply into the pipe, before it is accelerated by the cross flow and buoyancy effects in the upward direction. For the 5-mm injector, this value is reduced about 6 fold, so that buoyancy forces and the main liquid flow dominate the

problem, yielding jet trajectories (and deflection angles) that do not vary much for all three injection angles.

The deflected gas jets for twelve different conditions (four flow rates and three injection angles) are shown in Fig. 7. The marked boundaries were obtained through long exposure photographs. The most complex jet trajectory is given by the condition of Fig. 7b. As mentioned before, the direct impact of the gas jet onto the opposite wall for all the injection angles is notable, resulting in flow configurations that are highly dependent on γ.

4.3. Bubble morphology

4.3.1. Bubble size distribution

The size distributions of *small* bubbles for the 2 and 5-mm injectors and all flow conditions are shown in Fig. 8. The prominent feature is that in general the distributions seem to be insensitive to changes in the diameter and inclination of the injectors and also to the gas flow rates. The increase in the liquid flow rate resulted in the relative increase of small bubbles. This was indeed an expected trend, dictated by the increase in turbulent kinetic energy and shear rates—important conditions for bubble disintegration (Hinze, 1955; Walter and Blanch, 1986; Celis et al., 2021; Rosero et al., 2022). Fig. 8 also indicates that for the orthogonal injection *and* the 5-mm injector, the frequency of observed small bubbles (d_{eq} < 0.5 mm) increases. Several phenomena contribute to the appearance of small bubbles including the shear effects of the cross flow and the increased level of turbulence in the jet wake.

The size distributions of *large* bubbles for the 2 and 5-mm injectors and all flow conditions are shown in Fig. 9. The general trend is that for the definition of the sizes of the large bubbles, the relevant parameters are the gas flow rate, the injector diameter *and* inclination. For the low Q_G, the size distributions are about the same and γ has little effect on the size distributions. However, for the high Q_G (= 2.15 m³ h⁻¹) it is clear that the matching-flow configuration results in larger bubbles (as compared with other γ's) for both 2 and 5-mm injectors. The influence of the injector diameter is also relevant: 5-mm injectors result in distributions of d_{eq} which are 10%–40% higher than those of 2-mm injectors.

4.3.2. Bubble diameter cumulative density function (cdf)

The cdf of bubble diameters are shown in Fig. 10 for the 2-mm injector. For the low Q_G (Fig. 10a and c) the curves are very similar, with small changes due to the injection angle and a gentle slope. Bubbles with d_{eq} < 5 mm occupy over 97% of the cdf. For the high Q_G (Fig. 10b and d), the curves are quite distinct for the low Q_L in the interval 2 mm < d_{eq} < 5 mm. In this range, the opposite-flow flow (red line) induces the appearance of larger bubbles. For the high Q_L, all cdf curves are very alike. The biggest bubbles, however, are normally observed for the matching-flow configuration, as mentioned before.

For the 5-mm injector, the bubble diameter cumulative density functions are sensitive to changes in γ, in particular, for the low Q_G (Fig. 11a,c). It appears that the orthogonal gas injection tends to result in the highest cdf level for all conditions in the range 5 mm < d_{eq} < 30 mm. The results show, for example, that for γ = −45°, bubbles with d_{eq} larger than 20 mm are required for a cdf over 90%. For the high Q_G (Fig. 11b,d), the effects of γ are less apparent, although it is still clear that the largest bubbles occur in the matching-flow configuration.

4.3.3. The shapes of small and large bubbles

Since all the previous results were described in terms of d_{eq}, a discussion on the shapes of the small and large bubbles is necessary. The shapes of bubbles can be expressed in relation to different shape factors. Here, we consider the aspect ratio Λ = a/b, where a is the characteristic major axis of the bubble and b the characteristic minor axis. Fig. 12a shows that for the low flow rates (gas and liquid) the 2-mm injector produces shapes of bubbles that are relatively independent
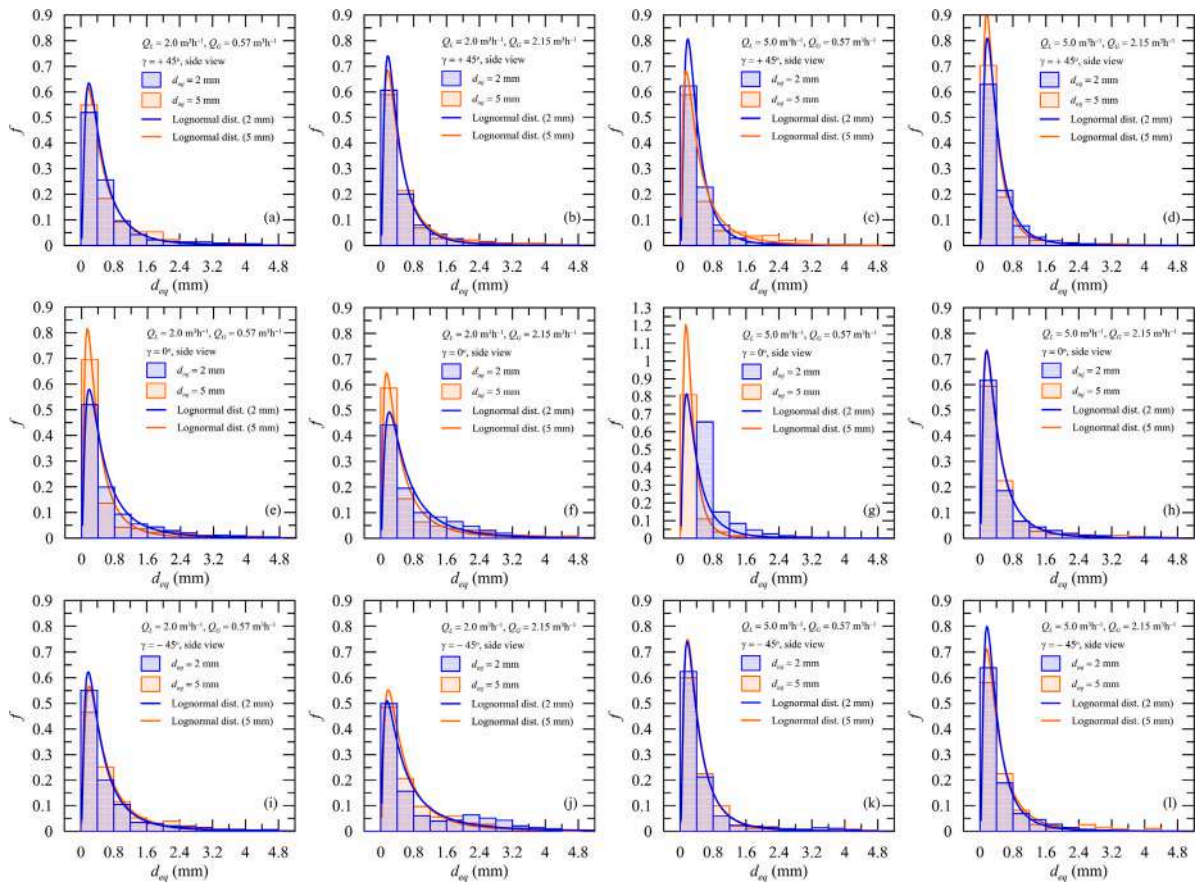
Fig. 8. Typical small bubble diameter distributions for the 2 and 5-mm injectors. All flow conditions.

of γ. For the small bubbles, Λ varies between 1 and 8, whereas for the large bubbles this variation is between 1 and 5. The distribution of points in Fig. 12a is, of course, strongly influenced by the pipe diameter (44-mm). Bubbles with d_{eq} of about 20 mm tend to exhibit Λ below 3, whereas bubbles with d_{eq} over 30 mm are stretched in the axial direction. An increase in the gas flow rate (Fig. 12b) results in two detached clusters of points: one for bubbles with $d_{eq} < 10$ mm and another for $d_{eq} > 50$ mm. Parameter Λ for the large bubbles varies between 3 and 5.

For the 5-mm injector and the low flow rates (Fig. 12c), most bubble equivalent diameters are below 40 mm. In all configurations, most Λ are below 5. This is in contrast with the high flow rates where very elongated bubbles are observed with Λ typically varying between 4 to 7 (40 mm $< d_{eq} < 60$ mm).

5. Continuous phase

5.1. Mean velocity profiles

Particle image velocimetry measurements of the water mean velocity profiles (u_z) are shown next in Figs. 13 through 15 for the 2 and 5-mm injectors. Profiles obtained through the *side view in a mid-pipe axial plane* are also shown. The mean velocity profiles are made non-dimensional with reference to U_{SL} (U_{SL} = superficial liquid velocity = Q_L/A).

For the 2-mm injector and conditions $Q_L = 2$ m³ h⁻¹, $Q_G = 0.57$ m³ h⁻¹, the opposite-flow and orthogonal injections result in relatively similar u_z profiles at all four measuring positions, $z/D =$

−0.5, 0.5, 1.0 and 1.5 (Fig. 13a). Due to the action of the large bubbles, the peaks in velocities are off-centered (at $z/D = 0.5$), but as the flows progress downstream, the peaks shift towards $x/D = 0.5$. The near wall large bubbles resulting from the matching-flow injection increase and offset the peak of u_z to the left ($z/D = 0.5$). Further downstream, as the large bubbles move to the pipe center region, the velocity peaks also shift towards this region, seeking to establish symmetry.

As Q_G is increased to 2.15 m³ h⁻¹, changes in the incoming u_z for $\gamma = -45°$ are very large (Fig. 13b, $z/D = -0.5$). The flow in the center region of the pipe is retarded by the effects of the large bubbles that eventually occupy the region $0.6 < x/D < 1$. The velocity profiles associated with the other two gas injection modes are similar at $z/D = -0.5$. At $z/D = 0.5$ the velocity profile corresponding to the matching-flow injection is displaced to the left, but, at the other locations, the profiles are very similar.

An increase in Q_L to 5 m³ h⁻¹ for $Q_G = 0.57$ m³ h⁻¹ (Fig. 13c) keeps the large bubbles close to the wall, resulting in peaks of u_z at about $x/D = 0.2$, for all γ. For the condition $Q_L = 5$ m³ h⁻¹, $Q_G = 2.15$ m³ h⁻¹ (Fig. 13d), U_{SL} is still large enough to drag most of the large bubbles to the center-pipe region with $\gamma = -45°$ and 0° . The bubbles injected in the opposite-flow direction reach the opposite wall.

Front view velocity profiles for the 2-mm injector and conditions $Q_L = 2$ m³ h⁻¹, $Q_G = 0.57$ m³ h⁻¹ and $Q_L = 5$ m³ h⁻¹, $Q_G = 2.15$ m³ h⁻¹ are shown in Fig. 14. For the low flow rates, the flow accelerates in the central region of the pipe to skip over the large bubbles (Fig. 14a). The acceleration in the flow subjected to the opposite-flow gas injection is the most prominent.
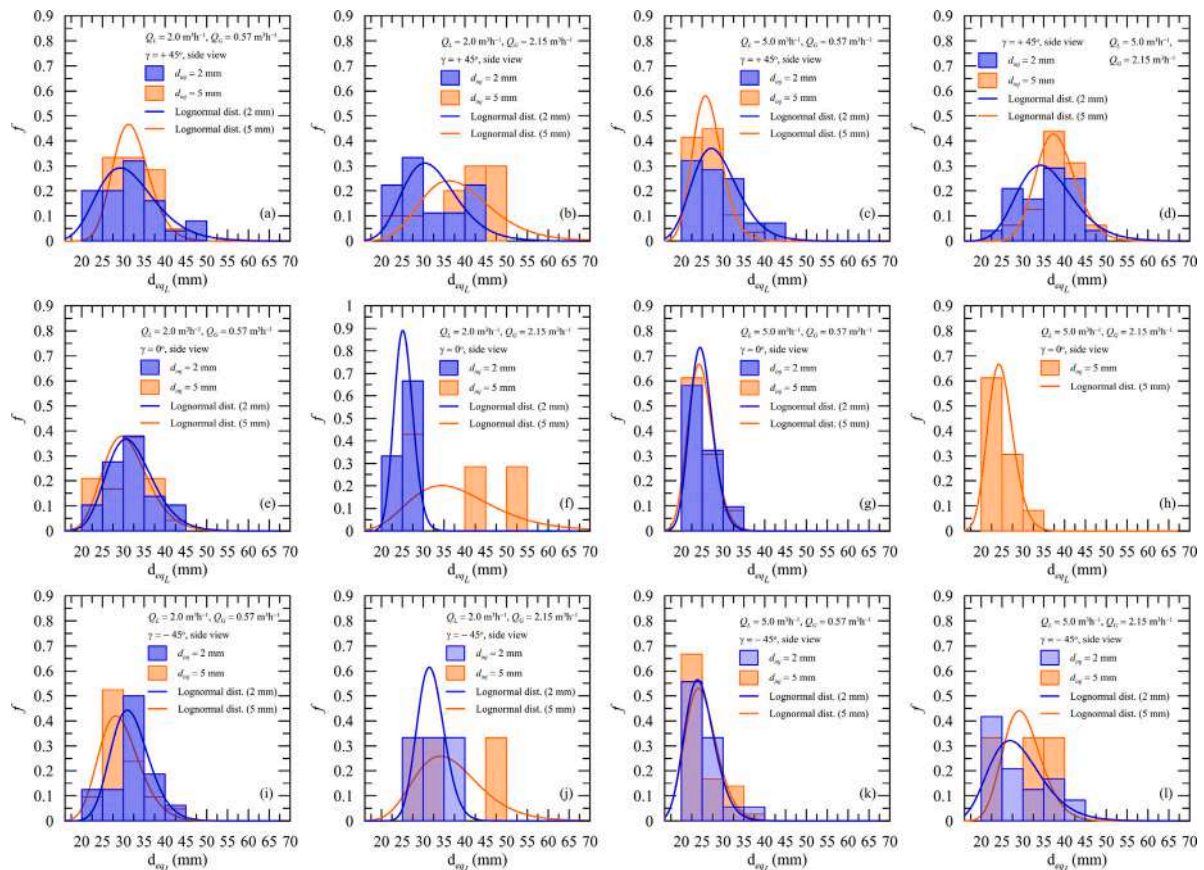
Fig. 9. Typical large bubble diameter distributions for the 2 and 5-mm injectors. All flow conditions.

The phenomenon is also observed for the high flow rates. However, the high Q_G (= 2.15 m³ h⁻¹) causes a large blockage by the bubbles, forcing the flow to divert sideways (Fig. 14b, $z/D = -0.5$).

Mean velocity profiles for the 5-mm injector are shown in Fig. 15, for four combinations of gas and liquid flow rates. For the 5-mm injector, the momentum flux of the injected gas is decreased for a given Q_L. The result, as pointed out before, is a small influence of γ on the flow pattern. This is clear in Figs. 15a,c,d. The mean velocity profiles in these figures, vary from position to position ($z/D = -0.5, 0.5, 1.0$ and 1.5), but exhibit similar trends. For $Q_L = 2$ m³ h⁻¹, $Q_G = 2.15$ m³ h⁻¹, the influence of γ is very strong, in particular, for $\gamma = 45°$ (Fig. 15b).

5.2. Pressure distribution

The effects of γ on pressure distributions are discussed next. Pressure differences were measured in the pipe length between the two pneumatic holdup valves, V_1 and V_3 (Fig. 2). The pressure taps were installed flush with the pipe at the top of valve V_1 and bottom of valve V_3. The distance between the two valves was 2 m. The arrangement described above resulted in a distance of 1.68 m between the pressure taps.

The gravitational pressure component (ΔP_G, Eq. (4)) was directly measured at the two quick release valves V_1 and V_3. A series of corrections were applied to the measured gas and liquid volumes to account for specific geometric details of the system (Rempto et al., 2015; Suarez, 2016; Guerra et al., 2017).

Figs. 16 and 17 show the behavior of ΔP_G for different liquid (Q_L) and gas (Q_G) flow rates for the three injection angles (γ). One evident

result is that as Q_G increases for a given Q_L the value of ΔP_G decreases. Another observation is that as γ changes from $-45°$ to $45°$, the pressure difference increases. This trend is particularly notable for the very high injection rates, over 2 m³ h⁻¹. For the lower injection rates (below 1.3 m³ h⁻¹) a reduction in ΔP_G is also noticed, but it is much less pronounced.

The combined effects of all pressure drop terms is shown in Figs. 18 and 19 (Eq. (3)). The apparent implication is that the beneficial (gravity) and detrimental effects (friction and acceleration) tend to cancel each other out yielding equivalent results. The present evidence is that the effects of γ on ΔP_{TOTAL} (Eq. (3)) are small. Over the whole range of tested conditions, the injection in all three directions resulted in almost equivalent results.

6. Conclusion

The present work discussed the properties of flow patterns that result from inclined gas injection into a vertical liquid column. Three different injection angles were examined for different gas and liquid flow rates and injector diameters. Optical measurements were used to determine the size distributions of small and large bubbles. The findings confirmed some expected results, in particular, that

- the 2-mm injector generates a considerable higher number of small bubbles as compared to the 5-mm injector,
- as a corollary to the above statement, bubbles formed by the 5-mm injector exhibit a bigger mean d_{eq} compared with the 2-mm injector.
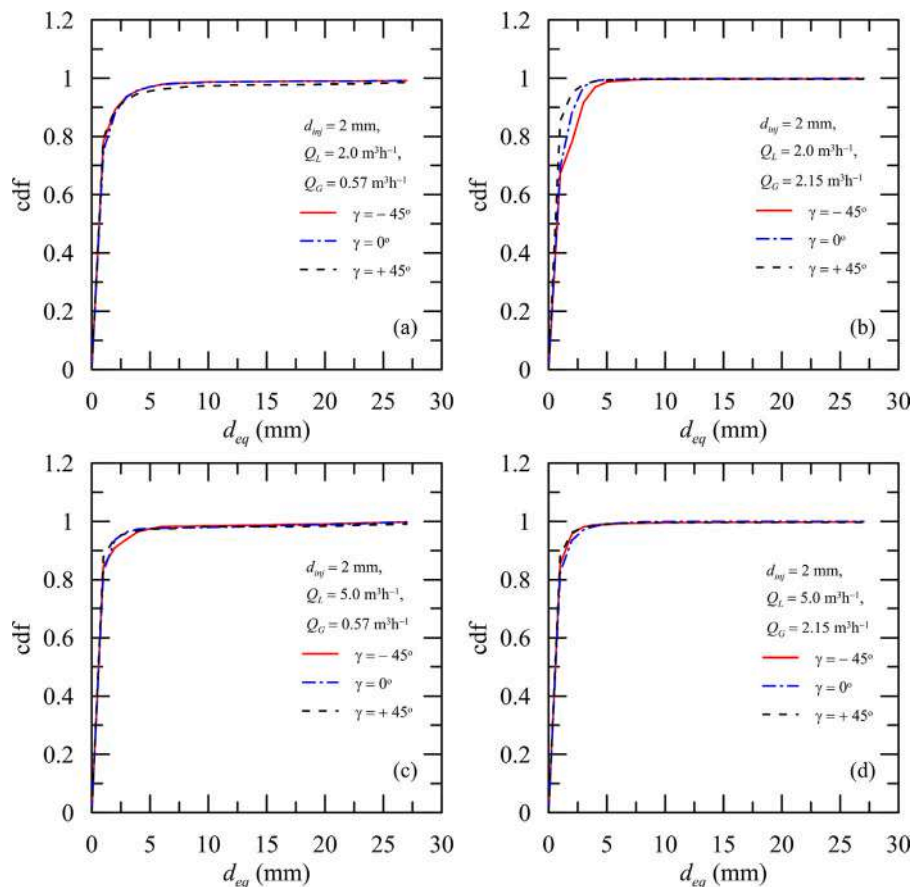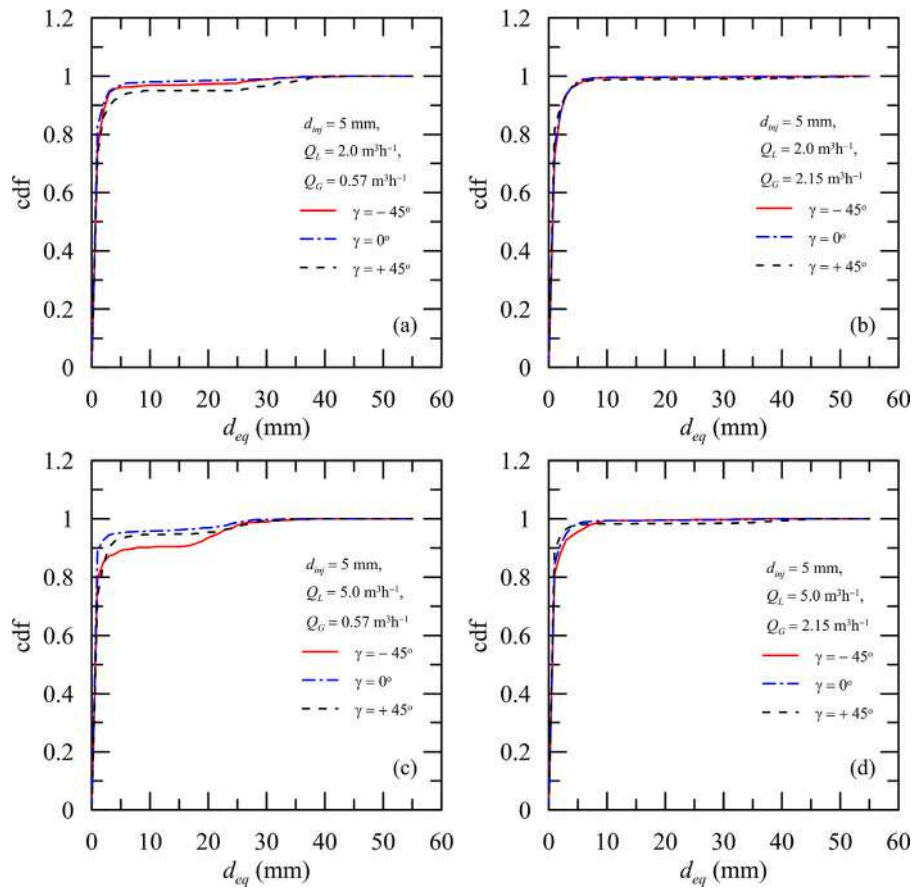
Fig. 10. Bubble diameter cumulative distribution. Matching-flow, orthogonal and opposite-flow directions for d_{inj} = 2 mm. (a) Q_L = 2 m³ h⁻¹, Q_G = 0.57 m³ h⁻¹; (b) Q_L = 2 m³ h⁻¹, Q_G = 2.15 m³ h⁻¹; (c) Q_L = 5 m³ h⁻¹, Q_G = 0.57 m³ h⁻¹; (d) Q_L = 5 m³ h⁻¹, Q_G = 2.15 m³ h⁻¹.

However, some new special features were also observed, as follow:

- The orthogonal injection tends to generate size distributions for the small bubbles with much higher peaks compared with the other two types of injection (matching-flow injection, opposite-flow injection).
- The 45° injection with the 5-mm injector tends to generate larger bubbles (again, compared with the other two injection geometry and for all flow rates).
- For the 2-mm injector, the above statement appears to be generally valid for high liquid flow rates (high Q_L).
- The mean liquid velocity profiles illustrate the interplay between Q_G and Q_L in determining the flow patterns since the peaks in the velocity profiles of the liquid phase are not symmetric due to the occurrence of large bubbles. These peaks mark the proximity of the bubbles to the near or far walls depending on the dominant effects of Q_G and Q_L.
- The changes in local pressure are small for all flow rates, meaning that in Eq. (3) the gravity, friction and acceleration terms balance each other, yielding almost equivalent effects.
- From the point of view of pressure difference, the opposite-flow injection provides better results for gas-lift applications (lower pressure differences).

CRediT authorship contribution statement

Declaration of competing interest

The authors declare that they have no known competing financial interests or personal relationships that could have appeared to influence the work reported in this paper.

Acknowledgments

Fig. 11. Bubble diameter cumulative distribution. Matching-flow, orthogonal and opposite-flow directions for $d_{inj} = 5$ mm. (a) $Q_L = 2$ m³ h⁻¹, $Q_G = 0.57$ m³ h⁻¹; (b) $Q_L = 2$ m³ h⁻¹, $Q_G = 2.15$ m³ h⁻¹; (c) $Q_L = 5$ m³ h⁻¹, $Q_G = 0.57$ m³ h⁻¹; (d) $Q_L = 5$ m³ h⁻¹, $Q_G = 2.15$ m³ h⁻¹.

Appendix A. Fluid mechanics of gas-lift systems

A.1. Momentum balance

Consider the control volume specified in Fig. A.1. For any given two positions 1 and 3, the balance of momentum equation can be written as

$$\frac{d}{dt} \int_W \rho \boldsymbol{u}\, dV + \int_{\partial W} \rho \boldsymbol{u}(\boldsymbol{u.n})\, dA = -\int_{\partial W} p \boldsymbol{n}\, dA + \int_W \rho \boldsymbol{b}\, dV + \int_{\partial W} \boldsymbol{\sigma.n}\, dA, \tag{1}$$

where W is the region of the fluid (with boundary ∂W), $\boldsymbol{u}$ denotes the fluid velocity, $\boldsymbol{n}$ is the unit normal of the surface of the control volume, ρ is the mass density, p is the pressure, $\boldsymbol{b}$ is a given body force per unit mass and $\boldsymbol{\sigma}$ is the stress tensor.

For one-dimensional (z-direction), steady flows, Eq. (1) reduces to

$$-(\rho_l u_{z_l}^2 A)_1 - \rho_g u_g^2 A_{inj} \sin\gamma + (\rho_L u_{z_l}^2 A_l)_3 + (\rho_g u_{z_g}^2 A_g)_3 = (p_1 - p_3)A$$
$$- Ag\left(\rho_l \int_1^2 dz + \int_2^3 ((1-\alpha)\rho_l + \alpha\rho_g)dz\right) \tag{2}$$
$$- \pi D \int_1^2 \tau_l dz - \pi D \int_2^3 \tau_m dz,$$

where the subscripts l and g denote the liquid and gas phases and m denotes the mixture. u_g and A_{inj} refer to the absolute velocity of the gas in the injection pipe and the cross section area. α is the local mean fraction of gas and τ the wall shear stress. The positions 1, 2 and 3 where the terms above need to be evaluated are indicated as per reference to Fig. A.1, g is the gravity acceleration. The angle γ is

referred to the x axis. In the position shown in Fig. A.1, $\gamma = -45°$ so that $\sin\gamma = -\sqrt{2}/2$ (negative); for a matching-flow direction, $\gamma = 45°$.

The problems in directly applying Eq. (2) are evident since α, A_l, A_g, τ_l and τ_m are unknown quantities difficult to determine.

A.2. Pressure

The balance of forces in Eq. (2) is sometimes presented in literature through the equivalent equation (Guet and Ooms, 2006)

$$\left[\frac{dP}{dz}\right]_T = \left[\frac{dP}{dz}\right]_g + \left[\frac{dP}{dz}\right]_f + \left[\frac{dP}{dz}\right]_a, \tag{3}$$

where the subscripts stand respectively for the effects of gravity, wall friction and fluid acceleration.

The gravity term can be evaluated from

$$\left[\frac{dP}{dz}\right]_g = -\rho_m g = -(\alpha\rho_g + (1-\alpha)\rho_l)g. \tag{4}$$

The wall friction term is normally estimated through an analogy with single-phase correlations of the form

$$\left[\frac{dP}{dz}\right]_f = -\lambda\rho_m \frac{2}{D} u_m^2, \tag{5}$$

where λ is the friction coefficient, ρ_m and u_m are the density and the velocity of the mixture.

The contribution of the acceleration term has been neglected by some authors with the argument that $\rho_g \ll \rho_l$ (Guet and Ooms, 2006). This term, however, can be approximated through equation,

$$\left[\frac{dP}{dz}\right]_a = -\frac{\rho_m}{2}\frac{du_m^2}{dz}. \tag{6}$$

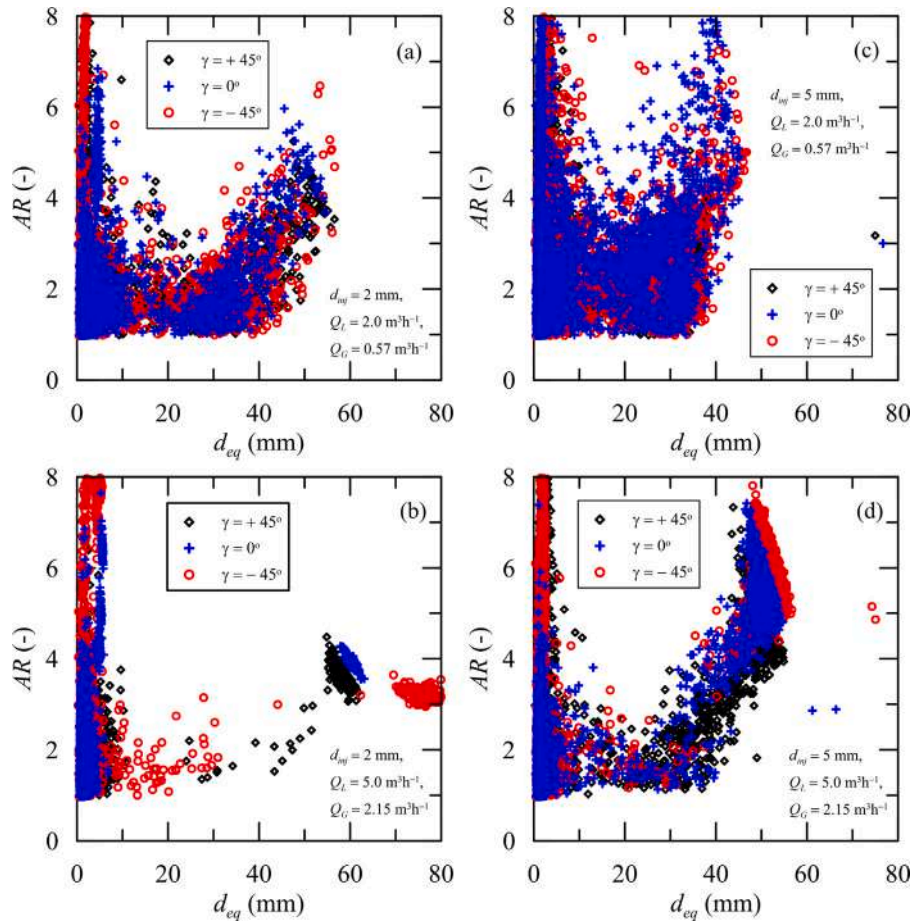where the mixture properties have been used to estimate the changes in acceleration.

Fig. 12. Aspect ratio of bubbles, 2 and 5-mm injectors. (a) $d_{inj} = 2$ mm, $Q_L = 2$ m^3 h^{-1}, $Q_G = 0.57$ m^3 h^{-1}; (b) $d_{inj} = 2$ mm, $Q_L = 5$ m^3 h^{-1}, $Q_G = 2.15$ m^3 h^{-1}; (c) $d_{inj} = 5$ mm, $Q_L = 2$ m^3 h^{-1}, $Q_G = 0.57$ m^3 h^{-1}; (d) $d_{inj} = 5$ mm, $Q_L = 5$ m^3 h^{-1}, $Q_G = 2.15$ m^3 h^{-1}.

For non-orthogonal gas injection, the total pressure drop is further affected by the additional *local* acceleration term (second term on the l.h.s of Eq. (2)),

$$[\Delta P]_a = \rho_g u_g u_{g_z} (d/D)^2. \tag{7}$$

where u_g is the absolute value of the gas injection velocity and u_{g_z} is the vertical projection of u_g.

All the terms in Eq. (3) are strongly affected by the manner in which gas is injected into the main pipe.

In principle, the gravitational term should always be reduced with an increase in the gas injection rate (Q_G). However, as Q_G increases, bubbles break and coalesce and changes in the flow pattern can be observed. All these effects have a large impact on the rise velocity of bubbles and their residence time. A reduction in bubble size generally delays bubbly to slug flow transition and increases their resident time with consequent beneficial effects for air-lift applications (Guet and Ooms, 2006).

In fact, for air bubbles in water in the spherical regime (diameters below about 1 mm, $R_b = 20$ (R_b = bubble Reynolds number)), a decrease in diameter always results in a decrease in terminal velocity. In the ellipsoidal regime, as the equivalent diameter increases, the terminal velocity of a bubble initially decreases, reaches a minimum (at about $d_{eq} = 6.5$ mm) and then increases again.

The other two terms in Eq. (3) increase with the increase in gas flow rate. Guet and Ooms (2006) also mention that since frictional losses typically account for less than 10% of the overall pressure gradient, the gravitational pressure term is the most relevant for gas-lift performance prediction.

Appendix B. Bubble size statistics according to the viewing angle

Bubble statistics for every flow condition were always gathered from two sets of data, obtained from side and front views of the injected gas.

For all liquid and gas flow rates, small bubbles immediately coming out of the 2-mm injector were better noticed through the side view. In the front view they tended to be obscured by the large bubbles but, of course, their exposition depended on the considered flow pattern (liquid and gas flow rates, injector diameter and angle). Typically the number of bubbles identified in the side view were over twice the number of bubbles observed through the front view. For the highest gas flow rate, and side view, the statistics for small bubbles were obtained from 6000 entries. Also, for high Q_G, statistics of large bubbles were difficult to obtain since the gas jet directly impacted the opposite wall resulting in a very complex flow pattern where large bubbles were surrounded by small bubbles. Under this condition, a clear definition of boundaries was not possible.

For the 5-mm injector, the number of recorded small bubbles was about one third of those recorded for the 2-mm injector for a given flow condition. The 5-mm injector, of course, tended to furnish larger bubbles which then appeared in smaller numbers. One peculiar aspect for the 5-mm injector was that for all injection angles and flow rates, the number of observed bubbles in the side and front views were about the same. Another noticeable fact was that for the orthogonal injection the number of observed small bubbles for the 2 and 5-mm injectors were comparable.

The size distributions of bubbles are next presented in terms of log-normal distributions as recommended by Gonçalves et al. (2018). Fig. B.1 shows the size distributions of small bubbles for side and front
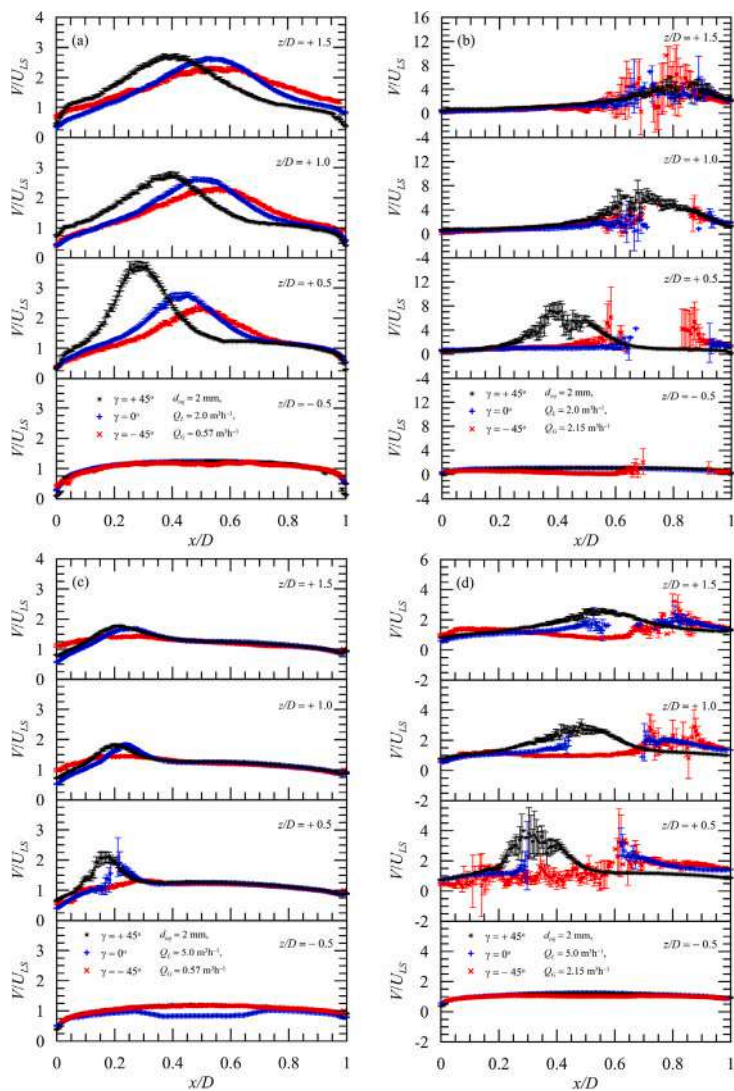
Fig. 13. Water mean velocity profile. Side view, d_{inj} = 2 mm. (a) Q_L = 2 m^3 h^{-1}, Q_G = 0.57 m^3 h^{-1}; (b) Q_L = 2 m^3 h^{-1}, Q_G = 2.15 m^3 h^{-1}; (c) Q_L = 5 m^3 h^{-1}, Q_G = 0.57 m^3 h^{-1}; (d) Q_L = 5 m^3 h^{-1}, Q_G = 2.15 m^3 h^{-1}. Black dots: matching-flow injection. Blue squares: orthogonal injection. Red triangles: opposite-flow injection.
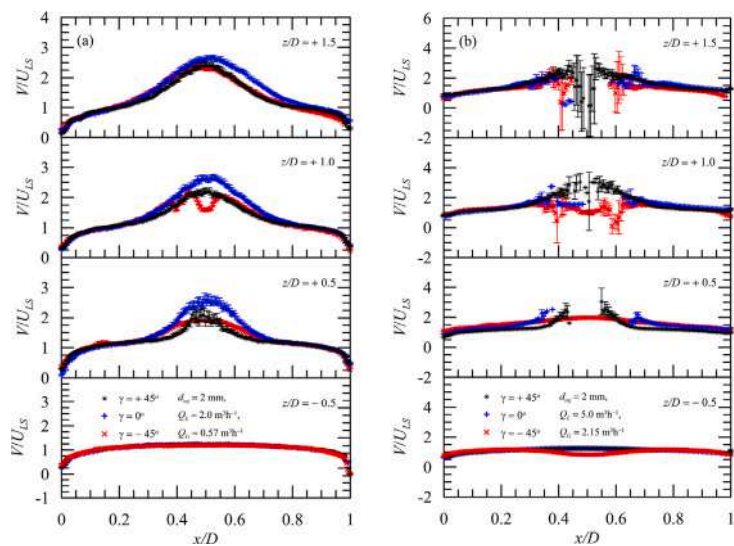

Fig. 14. Water mean velocity profile. Front view, d_{inj} = 2 mm. (a) Q_L = 2 m^3 h^{-1}, Q_G = 0.57 m^3 h^{-1}; (b) Q_L = 5 m^3 h^{-1}, Q_G = 2.15 m^3 h^{-1}.
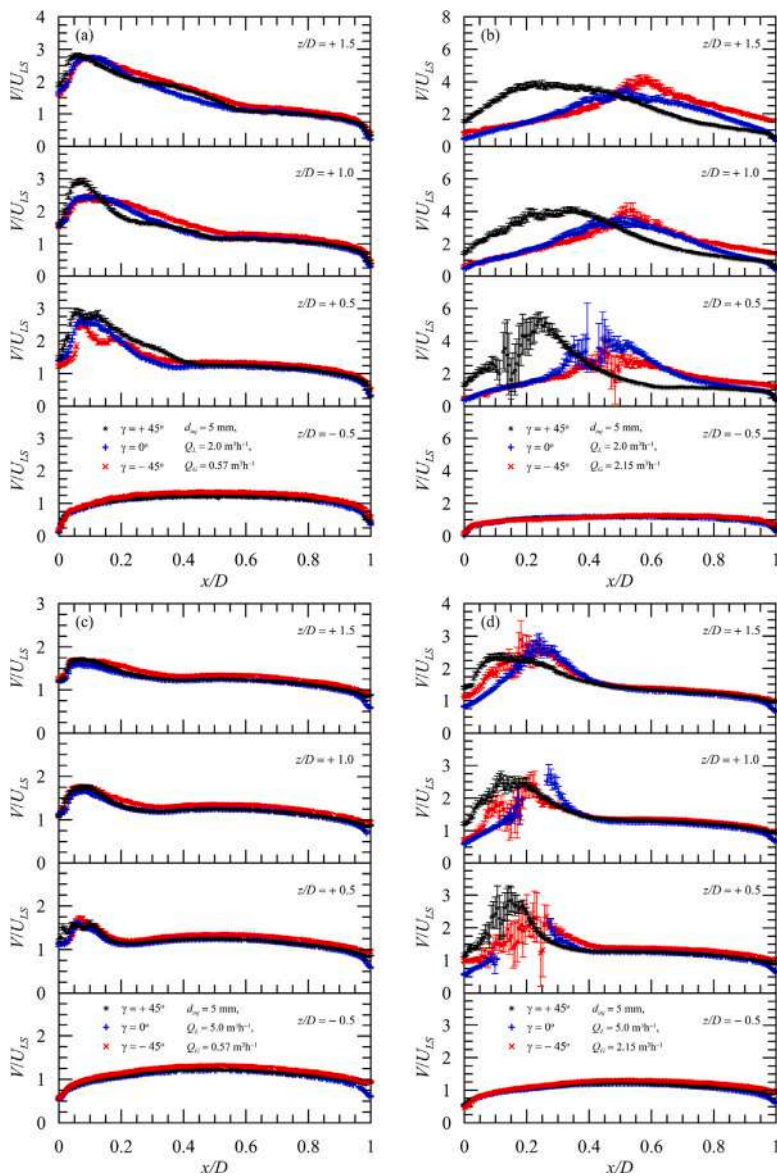
Fig. 15. Water mean velocity profile. Side view, d_{inj} = 5 mm. (a) Q_L = 2 m^3 h^{-1}, Q_G = 0.57 m^3 h^{-1}; (b) Q_L = 2 m^3 h^{-1}, Q_G = 2.15 m^3 h^{-1}; (c) Q_L = 5 m^3 h^{-1}, Q_G = 0.57 m^3 h^{-1}; (d) Q_L = 5 m^3 h^{-1}, Q_G = 2.15 m^3 h^{-1}.
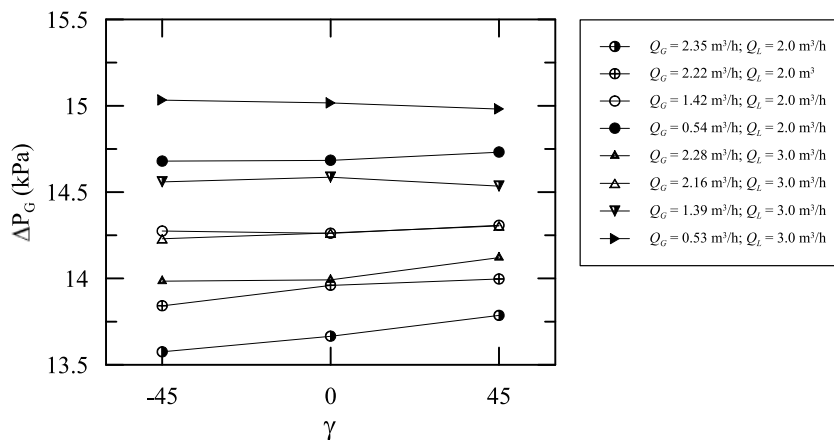
Fig. 16. Gravitational pressure drop for Q_L = 2 m^3 h^{-1} and 3 m^3 h^{-1}. The uncertainty for pressure measurements is 0.1%.
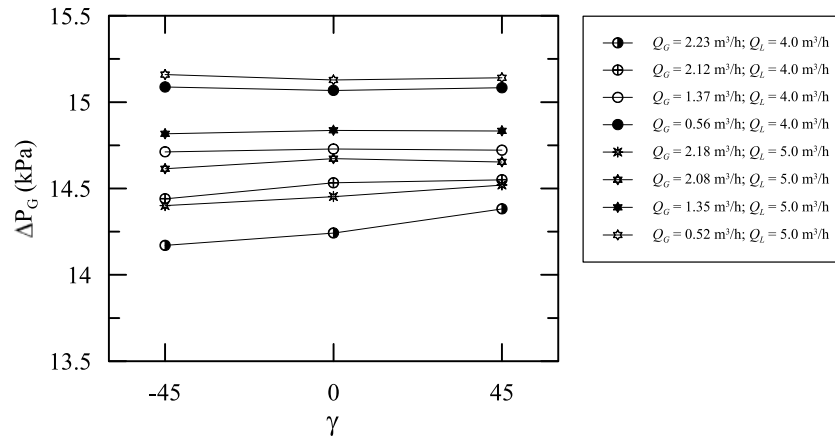
Fig. 17. Gravitational pressure drop for $Q_L = 4$ m^3 h^{-1} and 5 m^3 h^{-1}. The uncertainty for pressure measurements is 0.1%.

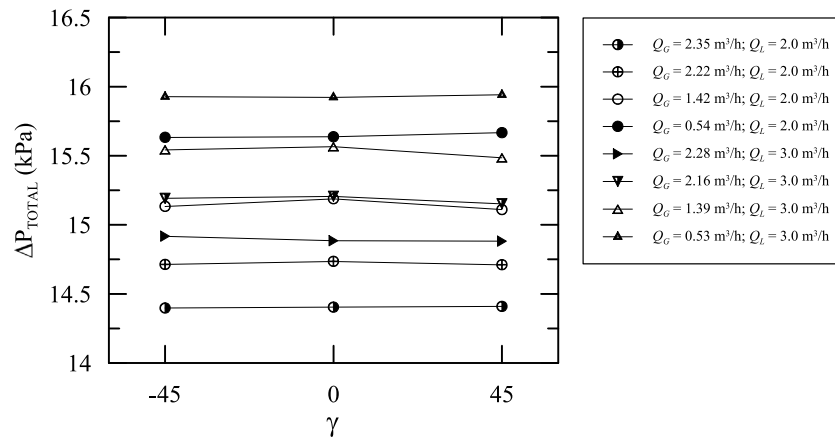**Fig. 18.** Total pressure difference for 2 m^3 h^{-1} and 3 m^3 h^{-1} liquid flow rates. The uncertainty for pressure measurements is 0.1%.

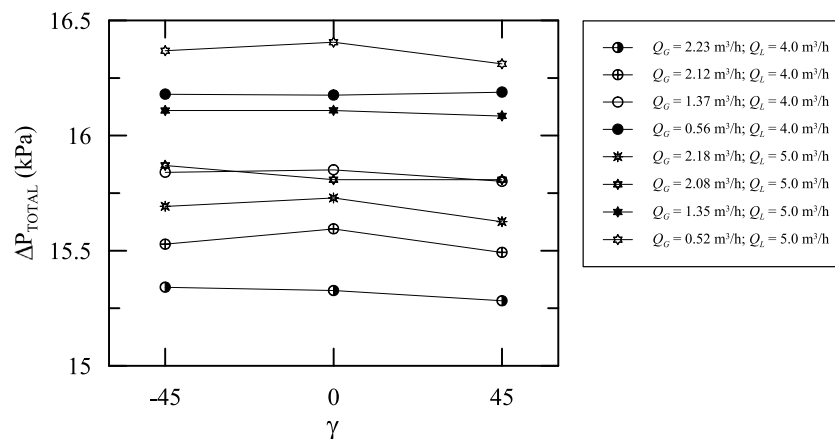**Fig. 19.** Total pressure difference for 4 m^3 h^{-1} and 5 m^3 h^{-1} liquid flow rate. The uncertainty for pressure measurements is 0.1%.
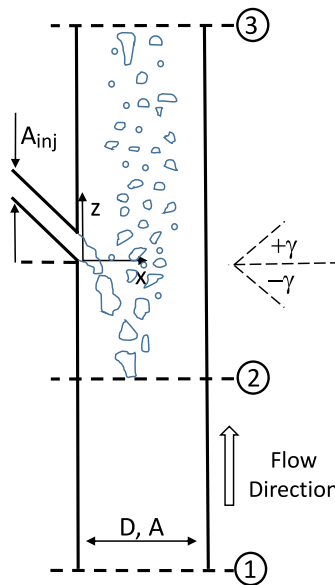
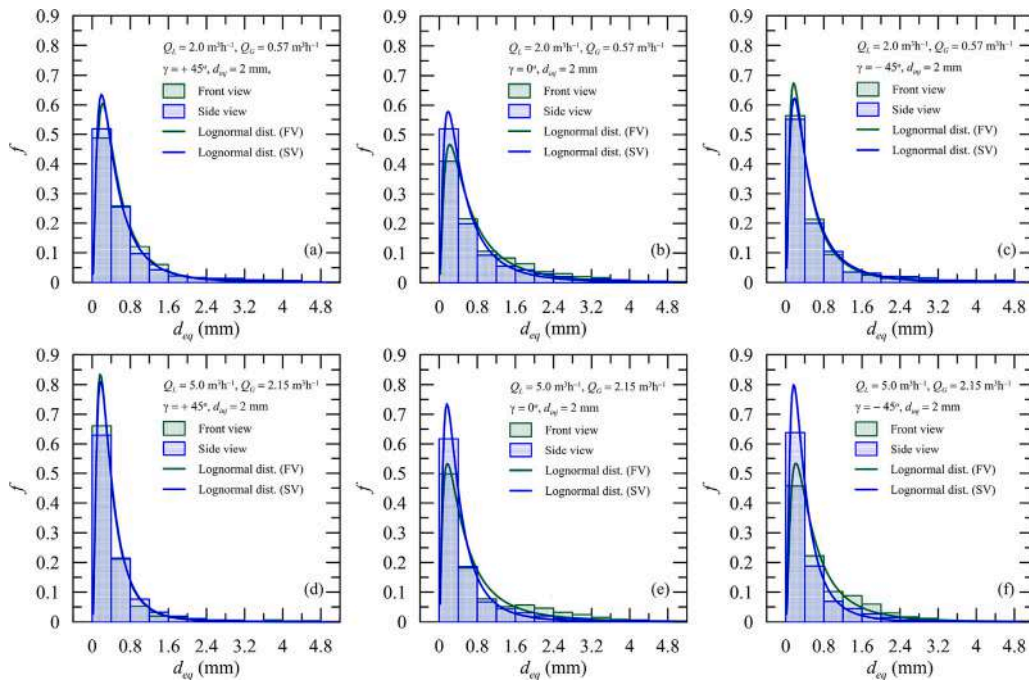**Fig. A.1.** Control volume for air-lift injector.

Fig. B.1. Small-bubble size distributions obtained from side and front views for a 2-mm injector, three injection angles and the opposite conditions $Q_L = 2$ m^3 h^{-1}, $Q_G = 0.57$ m^3 h^{-1} (low liquid and gas flow rates, a-b-c) and $Q_L = 5$ m^3 h^{-1}, $Q_G = 2.15$ m^3 h^{-1} (high liquid and gas flow rates, d-e-f).

views, all injection angles and two very distinct flow conditions: low flow rates of liquid and gas ($Q_L = 2$ m^3 h^{-1}, $Q_G = 0.57$ m^3 h^{-1}), and high flow rates of liquid and gas ($Q_L = 5$ m^3 h^{-1}, $Q_G = 2.15$ m^3 h^{-1}). The injector diameter is 2-mm. For most conditions the distributions are very similar. The most distinct situation is Fig. B.1f, where, as said before, small bubbles tended to be obscured by the large bubbles.

The size distributions for the large bubbles are shown in Fig. B.2, also for the 2-mm injector. The size distributions obtained with the side

view tended to give slightly higher average values of d_{eq}, but changes in standard deviations were small. In fact, the side-view projections normally resulted in slight higher lengths due to the inclination of the bubbles as they exited the nozzle. The number of entries for the statistics of the large bubbles was normally higher as the side view was considered.

Small bubble statistics obtained from side and front views with the 5-mm injector are shown in Fig. B.3, also for the two extreme
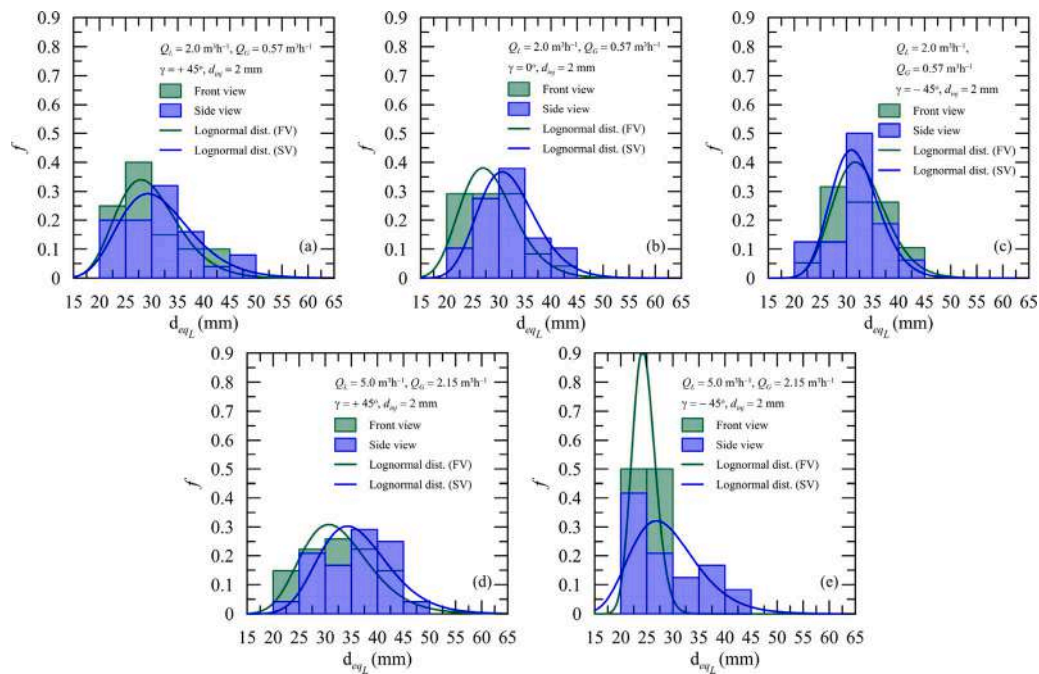
Fig. B.2. Large-bubble size distributions obtained from side and front views for a 2-mm injector, three injection angles and the opposite conditions $Q_L = 2$ m^3 h^{-1}, $Q_G = 0.57$ m^3 h^{-1} (low liquid and gas flow rates, a-b-c) and $Q_L = 5$ m^3 h^{-1}, $Q_G = 2.15$ m^3 h^{-1} (high liquid and gas flow rates, d-e). For the orthogonal injection and high flow rate ($Q_G = 2.15$ m^3 h^{-1}), bubble statistics were not obtained.
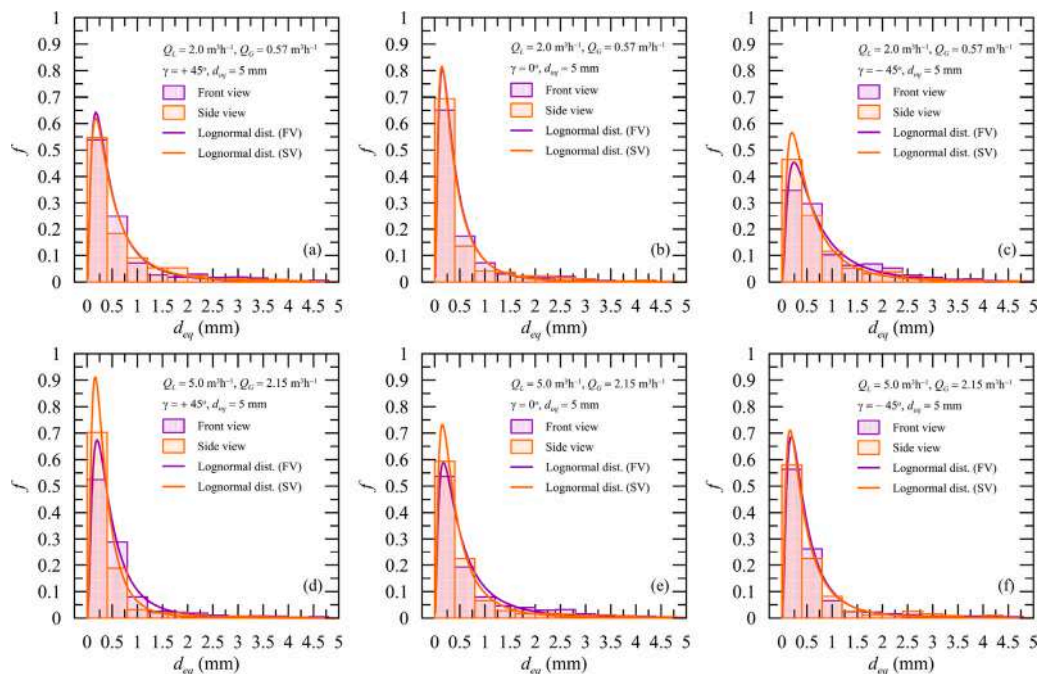

Fig. B.3. Small-bubble size distributions obtained from side and front views for a 5-mm injector, three injection angles and the opposite conditions $Q_L = 2$ m^3 h^{-1}, $Q_G = 0.57$ m^3 h^{-1} (low liquid and gas flow rates, a-b-c) and $Q_L = 5$ m^3 h^{-1}, $Q_G = 2.15$ m^3 h^{-1} (high liquid and gas flow rates, d-e-f).

conditions $Q_L = 2$ m^3 h^{-1}, $Q_G = 0.57$ m^3 h^{-1} and $Q_L = 5$ m^3 h^{-1}, $Q_G = 2.15$ m^3 h^{-1}. Much in the same manner as for the 2-mm injector, small bubbles tended to be blocked by large bubbles in the front view so that the distributions for the front view tended to show a greater number of larger bubbles. In any case, the distributions for all conditions are very alike.

For the large bubbles (Fig. B.4), the distributions for the low liquid and gas flow rates are similar. As the flow rates increase, the trend observed before for the 2-mm injector was further noted for the 5-mm injector: the side view tended to result in higher values of d_{eq} (by about 15%–18%), as expected.

Given the complexities of the flow patterns in all of the above considered cases, the differences in bubble size distributions were not considered significant. However, it appears from the above analysis that the distributions obtained with the side view are more representative of the problem in view of the larger number of entries and clearer bubble exposition. For this reason, the bubble size distributions described in this work were obtained with side-view data.
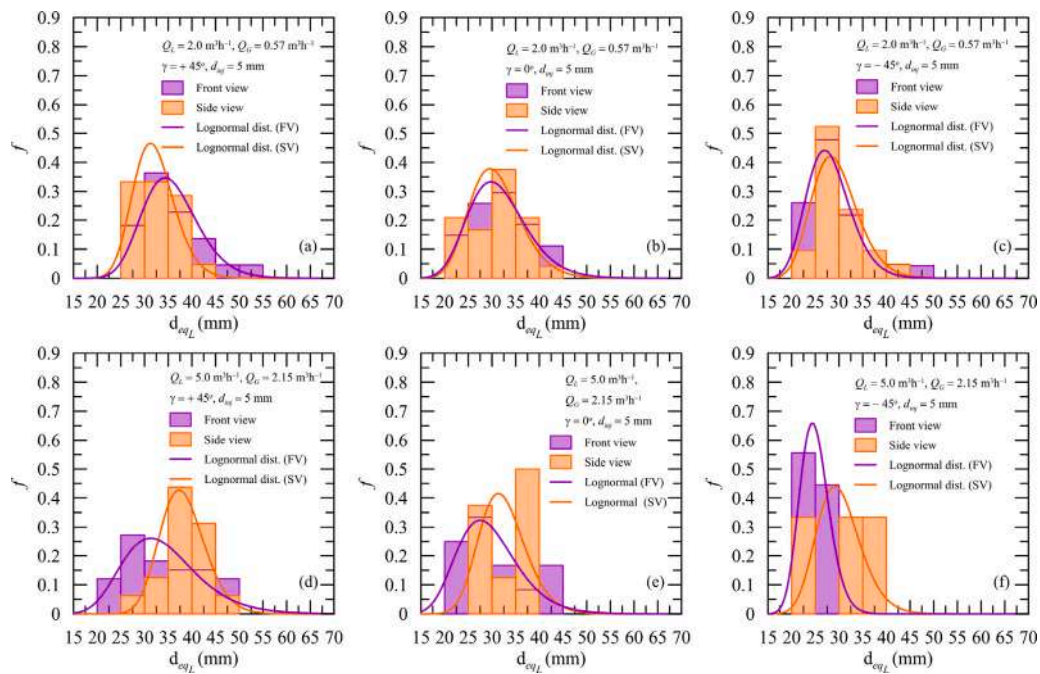
Fig. B.4. Large-bubble size distributions obtained from side and front views for a 5-mm injector, three injection angles and the opposite conditions $Q_L = 2$ m³ h⁻¹, $Q_G = 0.57$ m³ h⁻¹ (low liquid and gas flow rates, a-b-c) and $Q_L = 5$ m³ h⁻¹, $Q_G = 2.15$ m³ h⁻¹ (high liquid and gas flow rates, d-e-f).

References

Ahmed, W.H., Amanb, A.M., Badr, H.M., Al-Qutub, A.M., 2016. Air injection methods: The key to a better performance of airlift pumps. Exp. Thermal Fluid Sci. 70, 354–365.

Ayatollahia, S., Narimania, M., Moshfeghian, M., 2004. Intermittent gas lift in Aghajari oil field, a mathematical study. J. Pet. Sci. Eng. 42, 245–255.

Balachandar, S., Eaton, J.K., 2010. Turbulent dispersed multiphase flow. Annu. Rev. Fluid Mech. 42, 111–133.

Balzan, M.A., Sanders, R.S., Fleck, B.A., 2017. Bubble formation regimes during gas injection into a liquid cross flow in a conduit. Can. J. Chem. Eng. 95, 372–385.

Bezerra, M.F., Vigano, G.C., L., G.J., 2019. Optimization methodology of artifitial lift rates for Brazilian offshore field. In: Proceedings of Offshore Technology Conference, OTC-29889-MS. Rio de Janeiro, Brazil.

Brennen, C.E., 2005. Fundamentals of Multiphase Flow. CUP, Cambridge.

Brown, K.E., 1982. Overview of artificial lift systems. J. Pet. Technol. 2384–2396.

de Cachard, F., Delhaye, J.M., 1996. A slug-churn model for small-diameter airlift pumps. Int. J. Multiph. Flow. 22, 627–649.

Camponogara, E., Plucenio, A., Teixeira, A.F., Campos, R.V.S., 2010. An automation system for gas-lifted oil wells: Model identification, control, and optimization. J. Pet. Sci. Eng. 70, 157–167.

Celis, C.E.O., Rosero, C.M.P., Loureiro, J.B.R., Freire, A.P.S., 2021. Breakup and coalescence of large and small bubbles in sudden expansions and contractions in vertical pipes. Int. J. Multiph. Flow. 137, 103548.

Chen, K., Richter, H.J., 1997. Instability analysis of the transition from bubbling to jetting in a gas injected into a liquid. Int. J. Multiph. Flow. 23, 699–712.

Clift, R., Grace, J.R., Weber, M.E., 1978. Bubbles, Drops and Particles. Dover, New York.

Dhar, L., 2021. Étude de l´Injection d´Air à Travers des Fentes dans un Écoulement d´eau Transverse (MSc Thesis). Polytechnique Montreal.

Ferreira, A., Pereira, G., Teixeira, J.A., Rocha, F., 2012. Statistical tool combined with image analysis to characterize hydrodynamics and mass transfer in a bubble column. Chem. Eng. J. 180, 216–228.

Fu, Y., Liu, Y., 2016. Development of a robust image processing technique for bubbly flow measurement in a narrow rectangular channel. Int. J. Multiph. Flow. 84, 217–288.

Gonçalves, G.F.N., Baungartner, R., Loureiro, J.B.R., Freire, A.P.S., 2018. Slug flow models: feasible domain and sensitivity to input distributions. J. Pet. Sci. Eng. 169, 705–724.

Govier, G.W., Aziz, K., 1977. The Flow of Complex Mixtures in Pipes. Robert E. Krieger Publishing Company, New York.

Guerra, L.A.O., 2017. Experimental Analysis of the Effects of Gas Injection Angle on Vertical Liquid Flows (MSc Thesis). COPPE/UFRJ, (in Portuguese).

Guerra, L.A.O., Suarez, A.M.S., Loureiro, J.B.R., Silva Freire, A.P., 2017. Characterization of inclined gas jets in vertical liquid crossflows. In: Proceedings of the IV Journeys in Multiphase Flows (JEM2017). Sao Paulo, Brazil.

Guet, S.C.L., 2004. Bubble Size Effect on the Gas-Lift Technique (Ph.D. thesis). Technische Universiteit Delft, Delft.

Guet, S., Ooms, G., 2006. Fluid mechanical aspects of the gas-lift technique. Annu. Rev. Fluid Mech. 38, 225–249.

Hinze, J.O., 1955. Fundamentals of the hydrodynamic mechanism of splitting in dispersion processes. AIChE J. 3, 289–295.

Hu, D., Tang, C.-L., Cai, S.-P., Zhang, F.-H., 2012. The effect of air injection method on the airlift pump performance. J. Fluids Eng. 134, 111302–1.

Kaji, R., Azzopardi, B.J., Lucas, D., 2009. Investigation of flow development of co-current gas-liquid vertical slug flow. Int. J. Multiph. Flow. 35, 335–348.

Karn, A., Ellis, C., Arndt, R., Hong, J., 2015. An integrative image measurement technique for dense bubbly flows with a wide size distribution. Chem. Eng. Sci. 122, 240–249.

Khalil, M.F., Elshorbagy, K.A., Kassab, S.Z., Fahmy, R.I., 1999. Effect of air injection method on the performance of an air lift pump. Int. J. Heat Fluid Flow 20, 598–604.

Kulkarni, A.A., Joshi, J.B., 2005. Bubble formation and bubble rise velocity in gas-liquid systems: a review. Ind. Eng. Chem. Res. 44, 5873–5931.

Lau, Y.M., Thiruvalluvan Sujatha, K., Gaeini, M., Deen, N.G., Kuipers, J.A.M., 2013. Experimental study of the bubble size distribution in a pseudo-2D bubble column. Chem. Eng. Sci. 98, 203–211.

Lehr, F., Millies, M., Mewes, D., 2002. Bubble-size distributions and flow fields in bubble columns. AIChE J. 48, 2426–2443.

Liu, T., Bankoff, S., 1993a. Structure of air-water bubbly flow in a vertical pipe -I. Liquid mean velocity and turbulence measurements. Int. J. Heat Mass Transfer 36, 1049–1060.

Liu, T., Bankoff, S., 1993b. Structure of air-water bubbly flow in a vertical pipe -II. Void fraction, bubble velocity and bubble size distribution. Int. J. Heat Mass Transfer 36, 1061–1072.

Liu, C., Liang, B., Tang, S., Min, E., 2013. The effects of orifice orientation and gas-liquid flow pattern on initial bubble size. Fluid Dyn. Transp. Phenom. 21, 1206–2013.

Lucas, D., Beyer, M., Szalinski, L., Schutz, P., 2010. A new database on the evolution of air-water flows along a large vertical pipe. Int. J. Multiph. Flow. 49, 664–674.

Ma, R., Wei, B., Wang, J., 2021. Theoretical study for bubble diameter prediction at detachment from an orifice in high liquid velocity cross-flow. J. Dispers. Sci. Technol. 1–10. http://dx.doi.org/10.1080/01932691.2021.1883054.

Magalhães, G.R., Gonçalves, G.F.N., Loureiro, J.B.R., Freire, A.P.S., 2013. An experimental investigation of the effects of gas solubility on the properties of horizontal slug flow. Int. J. Multiph. Flow. 50, 33–40.

Magnaudet, J., Eames, I., 2000. The motion of high-Reynolds-number bubbles in inhomogeneous flows. Annu. Rev. Fluid Mech. 32, 659–708.

Mahdiani, M.R., Khamehchi, E., Abolfazl, A.A.S.A., 2019. Optimizing and stabilizing the gas lift operation by controlling the lift gas specific gravity. J. Pet. Sci. Technol. 9, 46–63.

Marshall, S.H., 1990. Air Bubble Formation from an Orifice with Liquid Cross-Flow (Ph.D. thesis). University of Sydney.

Marshall, S.H., Chudasek, M.K., 1993. A model for bubble formation from an orifice with liquid cross-flow. Chem. Eng. Sci. 48, 2049–2059.

Matamoros, L.M.C., Loureiro, J.B.R., Freire, A.P.S., 2014. Length-area-volume of long bubbles in horizontal slug flow. Int. J. Multiph. Flow. 65, 24–30.

Matas, J.-P., Marty, S., Cartellier, A., 2011. Experimental and analytical study of the shear instability of a gas-liquid mixing layer. Phys. Fluids 23, 94112.

Nishikiori, N., Redner, R.A., Doty, D.R., Schmidt, Z., 1995. An improved method for gas lift allocation optimization. J. Energy Resour. Technol. 117, 87–92.

Nogueira, S., Sousa, R.G., Pinto, A.M.F.R., Riethmuller, M.L., Campos, J.B.L.M., 2003. Simultaneous PIV and pulsed shadow technique in slug flow: a solution for optical problems. Exp. Fluids 35, 598–609.

Palke, M., 1996. Nonlinear Optimization of Well Production Considering Gas Lift and Phase Behavior. Stanford University, Stanford.

Plucenio, A., Ganzaroli, C.A., Pagano, D.J., 2012. Stabilizing gas-lift well dynamics with free operating point. In: Proceedings of the 2012 IFAC Workshop on Automatic Control in Offshore Oil and Gas Production. Trondheim, Norway.

Prasad, V.K., Chatterjee, D., Singh, S.P., 2018. Numerical simulation of gas-bubble formation through two submerged orifices. Sādhanā 43, 1–15.

Qi, F.S., Yeoh, G.H., Cheung, S.C.P., Tu, J.Y., Krepper, E., Lucas, D., 2012. Classification of bubbles in vertical gas-liquid flow: Part 1 - An analysis of experimental data. Int. J. Multiph. Flow. 39, 121–134.

Redden, J.D., Sherman, T.A.G., Blann, J.R., 1974. Optimizing gas-lift systems. In: SPE 5150. pp. 1–13.

Reinemann, D.J., Parlange, J.Y., Timmons, M.B., 1990. Theory of small-diameter airlift pumps. Int. J. Multiph. Flow. 16, 113–122.

Rek, Z., Gregorc, J., Bouaifi, M., Daniel, C., 2017. Numerical simulation of gas jet in liquid crossflow with high mean jet to crossflow velocity ratio. Chem. Eng. Sci. 172, 667–676.

Rempto, M.J., Suarez, A.M.S., Loureiro, J.B.R., Silva Freire, A.P., 2015. An experimental assessment of the fluid dynamics of gas lift mandrels. In: Proceedings of the SPE Artificial Lift Conference - Latin America and Caribbean. Salvador, Brazil.

Rosero, C.M.P., Celis, C.E.O., Loureiro, J.B.R., Freire, A.P.S., 2022. Phenomenology of bubble breakup and coalescence in sudden expansions and contractions in vertical pipes. Int. J. Multiph. Flow. 146, 103840.

Serizawa, A., Kataoka, I., Michiyoshi, I., 1975a. Turbulence structure of air air-water bubbly flow - I. Measuring techniques. Int. J. Multiph. Flow. 2, 221–223.

Serizawa, A., Kataoka, I., Michiyoshi, I., 1975b. Turbulence structure of air air-water bubbly flow - II. Local properties. Int. J. Multiph. Flow. 2, 235–246.

Serizawa, A., Kataoka, I., Michiyoshi, I., 1975c. Turbulence structure of air air-water bubbly flow - III. Transport properties. Int. J. Multiph. Flow. 2, 247–259.

Suarez, A.M.S., 2016. Experimental Study on the Effects of Gas Injection on Vertical Liquid Flows (MSc Thesis). COPPE/UFRJ, (in Portuguese).

Tavlarides, L.L., Coulaloglou, C.A., Zeitlin, M.A., Kinzing, G.E., Gal-or, B., 1970. Bubble and drop phenomena. Ind. Chem. Eng. 62, 6–27.

Wallis, G.B., 1969. One-Dimensional Two-Phase Flow. McGraw-Hill, New York.

Walter, J.F., Blanch, H.W., 1986. Bubble break-up in gas-liquid bioreactors: break-up in turbulent flows. Chem. Eng. J. 32, B7–B17.

Wang, Y., Dai, Z., Liu, H., 2021. Pore-scale mechanisms and simulations for gas-water two-phase transport processes in natural gas reservoirs. J. Nat. Gas Sci. Eng. 96, 104314.

Wang, P., Litvak, M., 2004. Gas lift optimization for long-term reservoir simulations. In: SPE 90506. pp. 1–8.